

THREE-DIMENSIONAL MEASUREMENT OF ATOMIC FORCE MICROSCOPE
CANTILEVER DEFORMATION TO DETERMINE THE THREE-DIMENSIONAL
APPLIED FORCE VECTOR

By

LEE KUMANCHIK

A DISSERTATION PRESENTED TO THE GRADUATE SCHOOL
OF THE UNIVERSITY OF FLORIDA IN PARTIAL FULFILLMENT
OF THE REQUIREMENTS FOR THE DEGREE OF
DOCTOR OF PHILOSOPHY

UNIVERSITY OF FLORIDA

2010

© 2010 Lee Kumanchik

To my mom and dad

ACKNOWLEDGMENTS

I thank my parents, Dwight and Bunny Kumanchik, for their support and for encouraging my dreams. I thank my love, Carolina Cardoza. If I have fire in my eyes it's because she lit fire under my feet. I thank my three aces, Steve, Alex, and Joel, who were just good old-fashioned entertainment. I thank the members of my committee and my advisor, Tony Schmitz, who is the most patient man I know. And I thank my peers in the Machine Tool Research Center for their shenanigans.

TABLE OF CONTENTS

	<u>page</u>
ACKNOWLEDGMENTS.....	4
LIST OF TABLES.....	7
LIST OF FIGURES.....	8
LIST OF ABBREVIATIONS	10
ABSTRACT.....	11
CHAPTER	
1 INTRODUCTION	13
The Atomic Force Microscope	13
The Detector	15
The Cantilever.....	18
Cantilever Dimensions	20
Force Application Location	21
Boundary Conditions.....	22
Traceability	23
The Force Equation	24
2 LITERATURE REVIEW	27
Historical Development.....	27
Applications of the Atomic Force Microscope	28
Force Modeling	29
Calibration	29
3 THREE-DIMENSIONAL IMAGING	33
A New Platform.....	33
Scanning White Light Interferometer.....	33
Cantilever Holders.....	35
Stages	36
Platform Assembly	37
Visualization of Quasi-static Bending.....	38
Residual Stress, “Batwings”, and Differencing	38
Snap-in	40
Other Experiments	41
4 THREE-DIMENSIONAL FORCE MODELING.....	44

5	VALIDATION OF THE FORCE MODEL	50
	Normal Loading.....	50
	Torsion Loading	58
	Uncertainty Analysis	63
6	CONCLUSIONS.....	68
	Summary.....	69
	Future Work	70
	LIST OF REFERENCES.....	71
	BIOGRAPHICAL SKETCH.....	76

LIST OF TABLES

<u>Table</u>	<u>page</u>
5-1. Cantilever geometries.....	59
5-2. Uncertainty contributions.....	64

LIST OF FIGURES

<u>Figure</u>	<u>page</u>
1-1. Schematic of atomic force microscope (AFM) operation.....	13
1-2. The optical lever technique.....	15
1-3. The small angle approximation.	16
1-4. A perfectly smooth sample slides past the stylus	17
1-5. Using the optical lever technique to detect twist.....	19
1-6. A scanning electron micrograph of a commercial cantilever.....	20
1-7. Cantilever stiffness transfer.	21
1-8. Foreshortening from vertical bending.....	23
1-9. Cantilever with a friction force proportional to the applied force, F	24
3-1. Prototype platform assembly.....	33
3-2. SWLI schematic.	34
3-3. Example cantilever placement on the aluminum holders (top views).	36
3-4. Positioning stage scale error.	37
3-5. The Olympus OMCL-AC240TS cantilever.	38
3-6. Olympus BL-RC150VB AB cantilevers.	39
3-7. Cantilever snap-in demonstration.....	41
3-8. Two Veeco 1930 (1.3 N/m, 35 μm wide) cantilevers in contact.....	41
3-9. Data dropout.	42
3-10. Tip wear estimation.....	43
3-11. Anomalous bending behavior.....	43
4-1. A cantilever loaded at the free end by two independent forces P and F	45
4-2. Force measurement does not depend on the global geometry of the cantilever. ...	45
4-3. The 3D view of the forces acting on the cantilever.....	46

4-4. SWLI measurement coordinates.	48
5-1. SWLI image of the fabricated cantilever.	50
5-2. Fabricated masses.....	51
5-3. Results of Equation 5-1 for the 10 masses.	53
5-4. Beam loaded under identical conditions, but measurement field of view was varied.	54
5-5. The aluminum “tee” bonded to a 1.5 mm wide cantilever.	56
5-6. Results of Equation 5-1 for the 8 masses using the surface fit approach.	57
5-7. “Tee” attached to cantilever.	58
5-8. Torsion results when mass is loaded at the positive torque arm.	60
5-9. Torsion results when mass is loaded at the negative torque arm.....	61
5-10. Torsion loading results for mass loaded at the positive and negative torque arms.	62
5-11. Normal loading results for mass loaded at the positive and negative torque arms.	62

LIST OF ABBREVIATIONS

AFM	Atomic force microscope
STM	Scanning tunneling microscope
SWLI	Scanning white light interferometer
SI	Système International d'Unités
3D	Three-dimensional

Abstract of Dissertation Presented to the Graduate School
of the University of Florida in Partial Fulfillment of the
Requirements for the Degree of Doctor of Philosophy

THREE-DIMENSIONAL DEFORMATION MEASUREMENT OF THE ATOMIC FORCE
MICROSCOPE CANTILEVER SENSOR FOR THE DETERMINATION OF THE
APPLIED FORCE VECTOR

By

Lee Kumanchik

August 2010

Chair: Tony Schmitz
Major: Mechanical Engineering

The atomic force microscope (AFM) is the instrument of choice for measuring nano- to micro-Newton forces (10^{-9} to 10^{-6} Newtons). However, calibration is required for accurate measurements. AFM calibration has been studied for decades and remains a significant focus within the metrological community, in particular at international standards organizations. While progress has been made, there is still much to accomplish as current force calibration techniques yield relative uncertainties (± 1 standard deviation/mean) of 10%-20%. For example, measuring a force of 500 nN would yield a result between 400-600 nN 68% of the time. The critical issue is the existing AFM metrology, which monitors deformation at a single (spatial) point on a structure that encounters a three-dimensional (3D) force and responds with a 3D deformation. This single-point calibration technique considers only a limiting set of information, while additional information is available. Similarly, subsequent measurements by the AFM after calibration are restricted to the same limits. As a response, this project aims to improve AFM calibration and use by implementing a new metrological platform and analysis technique.

The new platform incorporates a scanning white light interferometer (SWLI) for 3D cantilever deformation measurements. The SWLI introduces two important changes over standard AFM metrology. First, it provides a multi-point measurement of the backside surface of the cantilever rather than a single-point measurement near the free end. Second, it is a direct displacement sensor which does not infer displacement from the measurement of another variable, such as the surface angle in the optical lever technique. In this study, the AFM is first described with a focus on its use as a force sensor. Then, the new platform design and construction, cantilever imaging tests, and the development of a new force model, which takes advantage of the 3D deflection data, are presented. The new force model addresses many of the challenges associated with traditional calibration strategies. Experimental validation is presented for the cases of “normal” force loading (i.e., perpendicular to the cantilever axis and resulting in bending deformation) and “torsional” loading.

CHAPTER 1 INTRODUCTION

The Atomic Force Microscope

The atomic force microscope (AFM) is a multipurpose instrument used for interacting with a sample at an atomic scale (including imaging, force interaction, and manipulating individual atoms). Interaction is performed by an atomically sharp stylus that is driven by stages to a location of interest on a sample. The small tip radius of the stylus (<30 nm or approximately the radius of a virus) focuses the interactions onto a small (nearly point) area enabling extremely fine spatial resolution. The stylus is attached to a cantilever that is monitored by a detector as it deforms under the interaction forces (Figure 1-1). Although the entire cantilever deforms, the detector typically determines the motion at or near the stylus (located at the free end of the cantilever) only. This is a natural choice since the AFM can perform imaging with the stylus motion having a 1:1 correlation (ideally) to a sample's surface contours. When used for force measurement, the stylus motion follows Hooke's law, $F=ky$, where F is the vertical force, k is the cantilever bending stiffness, and y is the stylus vertical displacement. Using an AFM, force resolution as low as 1 pN (10^{-12} N) can be realized.

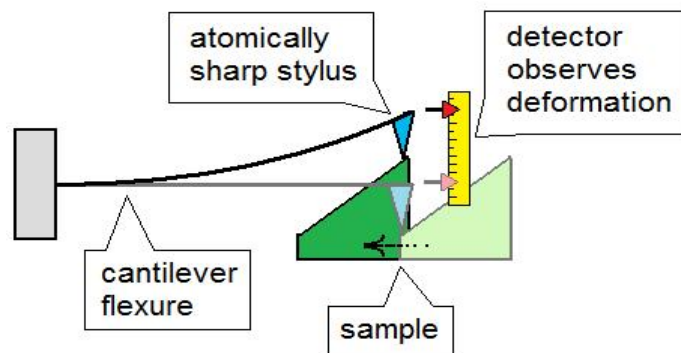


Figure 1-1. Schematic of atomic force microscope (AFM) operation. Forces at the stylus from the moving sample cause deformation in the cantilever. A detector observes the deformation.

Due to the AFM's popularity as a multi-function instrument, it is applied across a diverse range of disciplines where users often may not possess detailed knowledge of the underlying mechanics. Therefore, vendors strive for "turn key" system operation. However, achieving the required accuracy under this paradigm can be challenging. For example, cantilever stiffness studies have found that the manufacturer-specified stiffness can vary by as much as 300% from the calibrated stiffness (0.2 N/m nominal stiffness vs. 0.067 N/m calibrated stiffness) [1]. One study combined all manufacturer specifications required for force measurement (including stiffness) and found the combined uncertainty was greater than 1500% [2]. While this level of divergence may not always be present, calibrating the AFM is clearly required to obtain meaningful results. However, after decades of calibration research, the best stiffness calibrations, performed by international standards agencies, are accurate to only 5% [3]. Using methods available to the average user, the accuracy of stiffness calibration is limited to 10%-20%, in general [2,4]. Because stiffness is one of the parameters required to determine force, the accuracy of the force measurement will be no better than the stiffness accuracy and, most likely, will be worse.

Since the force is computed with Hooke's law ($F=ky$), there are two components to a force calibration: 1) stylus displacement calibration; and 2) stiffness calibration, with the majority of research focused on stiffness calibration. This force relation, however, is too simplistic. Cantilever mechanics studies have shown how cross-axial sensitivity to forces perpendicular to the measurement direction lead to a systematic error between 10%-20% [5]. This error is independent of calibration. While compensatory post-processing techniques are available [6], they are largely unused for several reasons.

First, their complexity requires expertise in mechanics to understand and programming knowledge to implement. Second, they require the geometrical parameters of the AFM setup (which are often difficult to obtain) and knowledge of the stylus-sample interactions (which are typically unknown *a priori*). Third, they continually evolve and must be updated every couple of years [5-8]. Therefore, the simple force equation, $F=ky$, remains in use. In a comprehensive review (1254 cited references) of AFM calibration and implementation in numerous fields, there was no mention of any alternative force relation to $F=ky$ [9]. In the following sections, force measurement by AFM is discussed in three parts: the detector, the cantilever, and the force equation.

The Detector

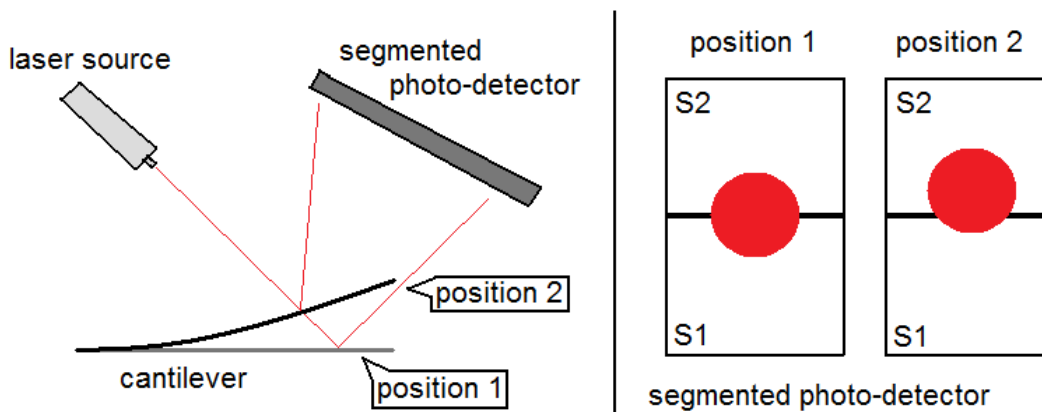


Figure 1-2. The optical lever technique. A laser is reflected off a cantilever onto a photo-detector. The light level on each segment of the photo-detector (S1 and S2) represents the amount of cantilever deflection.

The stylus displacement (perpendicular to the cantilever axis in the “normal” force direction) is monitored by a detector (represented by y in $F=ky$). The most popular detection system in use today is the optical lever technique (Figure 1-2). Here, a laser is reflected from the backside of a cantilever onto a two-segment photo-detector. As the cantilever deforms, the angle of incidence changes and the reflected laser beam moves

along the photo-detector segments. The light levels on the segments are directly related to the angle of incidence of the cantilever (after compensating for photo-detector non-linearity). The longer the optical path, the more pronounced the effect; this amplification follows the simple lever rule. Though detection is directly related to angle, it is difficult to calibrate for angular motion. Additionally, in imaging mode and when applying Hooke's law, the vertical displacement (not cantilever angle) is required. Therefore, a rigid surface calibration is typically performed. Here, the stylus is brought into contact with a rigid sample and then the sample stage is displaced vertically. Using the known commanded displacement, the small angle approximation can be used to determine a rate of displacement directly proportional to the angular change of the AFM cantilever (Figure 1-3). In this way, the stylus vertical displacement accuracy is approximately equal to the stage vertical displacement accuracy.

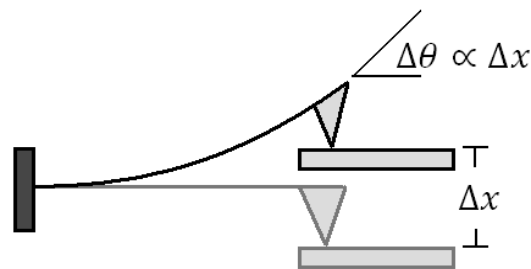


Figure 1-3. The small angle approximation. Small deformations enable the cantilever angular change to be related to the stage vertical motion.

While this detection system is simple in practice, it suffers from a critical drawback. Since it indirectly measures displacement through angular change, any force which causes the cantilever to deform without displacing the stylus vertically will still register as stylus motion. For example, a sample moving parallel to the beam axis while in contact with the stylus will generate a kinetic friction force that will tend to deform the cantilever flexure (Figure 1-4). Though the sample may be perfectly smooth (no

topography), the lateral friction will register as vertical motion due to the change in reflected beam angle. This phenomenon has been exploited in tribology since bi-directional motion registers as complementary positive and negative detector output that relates to friction [10]. As an alternative to motion parallel to the beam axis, perpendicular motion can also be used to measure friction. This motion causes beam twist (torsional loading) and can be measured using a quadrant photo-detector (Figure 1-5). The arrangement of four total segments isolates twist from stylus vertical displacement so that topography is not registered as friction in the twist direction. The challenge is

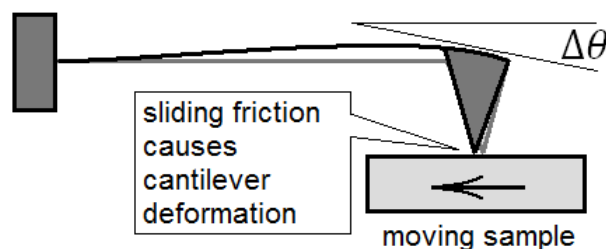


Figure 1-4. A perfectly smooth sample slides past the stylus. The resulting friction force deforms the cantilever which registers as motion by the detector.

that twist is a measure of angle and therefore requires a more complex calibration compared to the rigid surface calibration used for displacement. Additionally, twist angle is proportional to torsion (i.e., the product of the friction force and stylus length), not just the frictional force. Therefore, the stylus length (or height) must be measured to calculate the frictional force.

Calibrating the detector for every measurement is essential for obtaining good force accuracy. In practice, however, this may not be practical. In the absence of comprehensive calibration, misalignment between the detector and the cantilever may

go undiagnosed. For the optical lever technique, the angle of incidence determines the displacement, which imparts some robustness to misalignment. The angular deflection equation for a rectangular cantilever with an end force and its sensitivity to measurement location are,

$$\theta(x) = \frac{3F}{2L^3k}(2Lx - x^2) \quad \& \quad \frac{\partial\theta}{\theta} = \frac{2Lx-2x^2}{2Lx-x^2} \frac{\partial x}{x} \quad (1-1)$$

where L is the cantilever length, x is the location along the beam axis ($0 \leq x \leq L$), and θ is the angle of the cantilever. Misalignment of the laser from the calibrated position gives an error rate in displacement measurement, $x:y$, between 1:1 and 1:0 from the base to free end, respectively. For example, a system calibrated for $x = L$, but misaligned by a few micrometers, would introduce virtually no error in corresponding displacement measurements due to this misalignment. Since this is the most common position to point the laser, the optical lever technique is fairly robust to misalignment. For AFM systems with direct displacement sensors such as displacement measuring interferometers, alignment errors are not mitigated but instead amplified. The deflection equation and sensitivity to measurement location for displacement are,

$$y(x) = \frac{F}{2L^3k}(3Lx^2 - x^3) \quad \& \quad \frac{\partial y}{y} = 3 \frac{2Lx^2-x^3}{3Lx^2-x^3} \frac{\partial x}{x} \quad (1-2)$$

Misalignment of the detector from the calibrated position gives an error rate, $x:y$, between 1:3 and 2:3 from base to free end with the free end being the best position.

The Cantilever

The cantilever is an interchangeable component in the AFM system. Cantilevers are made with different geometries and tips (in addition to sharp styli, spheres are also often used, for example) to suit many applications with the same AFM system.

Regardless of the cantilever manufacturer (often different from the AFM system

manufacturer), the bending stiffness is always specified for use in the force equation (k in $F=ky$). However, the stiffness is extremely sensitive to cantilever geometry and, therefore, must be calibrated on an individual basis. Potentially the most confounding issue faced by stiffness calibration is that the stiffness of a generalized beam depends on the boundary conditions. For example, a fully constrained (fixed/fixed) beam has four times the stiffness of a cantilever (fixed/free) beam. For the AFM cantilever, the stiffness estimation is naturally based on the cantilever model; the complexities that arise from the stylus contact mechanics, which alter the system stiffness, are left for the user to handle.

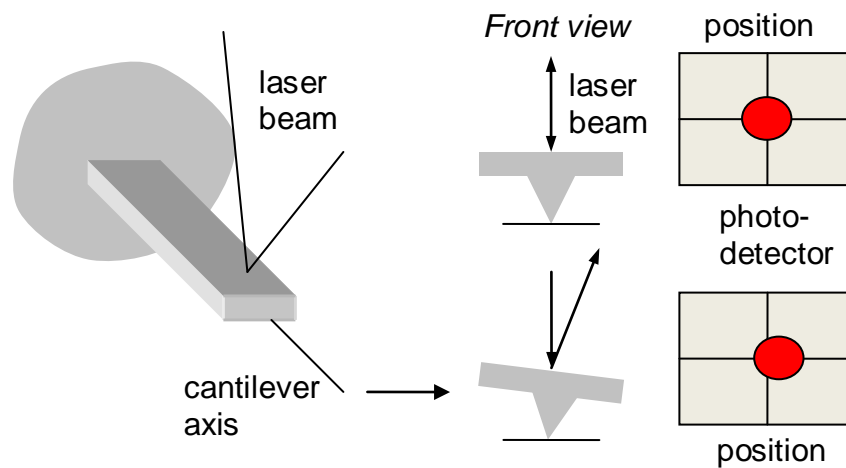


Figure 1-5. Using the optical lever technique to detect twist. The left-to-right motion of the laser registers as twist. The top-to-bottom motion registers as vertical deflection, as shown previously.

There are numerous stiffness calibration techniques and each has benefits and drawbacks. Non-contact techniques avoid stiffness altering contact mechanics, but do not take into consideration the load application location. Contact techniques are often simpler conceptually and more convenient for achieving traceability to international

standards, but must compensate for contact behavior. Rather than list the techniques here (see Chapter 2), the largest sensitivities to stiffness are described.

Cantilever Dimensions

A cantilever's dimensions define its stiffness. From solid mechanics, a rectangular cantilever beam can be modeled using Euler-Bernoulli beam theory. At the stylus, the deflection equation is,

$$y = \frac{4F}{Ew} \left(\frac{L}{t}\right)^3 \xrightarrow{\text{rearrange}} F = \overbrace{\frac{Ew}{4} \left(\frac{t}{L}\right)^3}^k y \quad (1-3)$$

where E is Young's modulus for the beam material, w is the beam width, L is the beam length, and t is the beam thickness. Rearranging yields an expression for the stiffness according to Hooke's law (analytical models exist for other beam geometries and can similarly be used to estimate stiffness). Direct measurement of each term provides the best result so that the stiffness uncertainty is a combination of the measurement

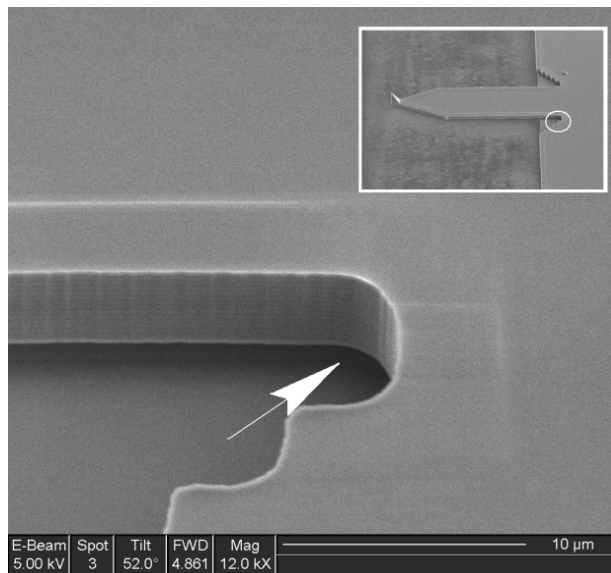


Figure 1-6. A scanning electron micrograph of a commercial cantilever. Extra material is cut away during manufacturing. This undercut is not visible in a top-down view of the cantilever.

uncertainties in each input and the model accuracy (i.e., considering the limitations imposed by the model assumptions). In this example, the most sensitive parameters are thickness and length. Thickness of silicon substrates (the typical AFM cantilever material) is difficult to predict from manufacturing and should be measured directly. Length can vary from nominal due to undercut at the base when using silicon-based manufacturing techniques (Figure 1-6). Assuming all other quantities are perfectly known, there is approximately a 1:3 relationship between the error in length or thickness to the error in stiffness. For example, a 1% error in thickness or length leads to an error in stiffness of ~3% (± 30 nm thickness error or ± 2 μm length error on a 3 μm x 200 μm cantilever with a nominal stiffness of 6 N/m gives a stiffness error of ± 0.18 N/m).

Force Application Location

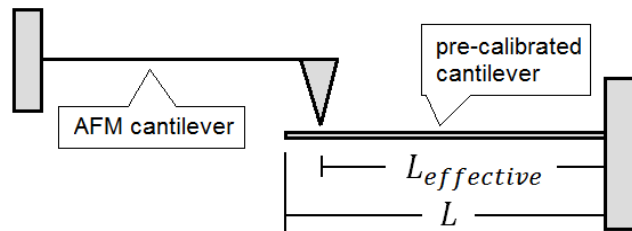


Figure 1-7. Cantilever stiffness transfer. The AFM cantilever is pushed against the pre-calibrated cantilever. The force application point on the AFM cantilever is precisely located at the stylus. However, the force application point on the pre-calibrated cantilever is subject to the position accuracy of the AFM. The effective length of the pre-calibrated cantilever determines the measured stiffness.

A more direct technique to determine stiffness is to apply a known force to the cantilever and measure the displacement so that $k=F/y$. For relatively stiff cantilevers, a mass can be attached to the free end to apply a known (gravity-based) force. Here, the force application point requires precise alignment to the stylus location, where the cantilever will experience all subsequent forces. The sensitivity to alignment errors is

identical to the length sensitivity with the same 1:3 relationship. For mass loading, there is a fundamental limitation imposed by the availability of traceable mass artifacts smaller than 1 mg. Therefore, a variation of the force loading scheme, referred to as a stiffness transfer, is used where the unknown stiffness of a cantilever is related to the pre-calibrated stiffness of a second cantilever. The result is similar to a system of two springs in series such that $k_1 = k_2(x_2/x_1 - 1)$ where k_1 is the unknown stiffness, k_2 is the known stiffness, x_2 is the total motion as one cantilever is pressed against the other, and x_1 is the response motion of the unknown cantilever. Here, the force application point on the unknown cantilever is determined precisely since the stylus makes direct contact with the cantilever of known stiffness. However, the force location on the second cantilever is again subject to alignment errors and results in an error in stiffness at a rate of 1:3 (Figure 1-7).

Boundary Conditions

For contact-style stiffness calibrations, as well as any use of an AFM cantilever after calibration, boundary conditions can contribute considerable measurement uncertainty. Boundary conditions define the deflection equation (the equations presented so far have been for an ideal cantilever with a vertical load at the stylus). This simplification fails when the cantilever comes into contact with a sample, either during contact style calibrations or when used to perform measurements. An example contact phenomenon is friction, as discussed previously. Foreshortening occurs whenever the cantilever deforms (Figure 1-8). The foreshortening is resisted by friction parallel to the sample surface. As an example, the stylus vertical motion for a cantilever experiencing sliding friction proportional to the vertical force is,

$$y = F \underbrace{\left[\frac{1 + \frac{3r}{2L}\mu}{k} \right]}_{\text{system compliance}} \quad (1-4)$$

where μ is the coefficient of kinetic friction and r is the stylus height. Assuming this to be the only boundary condition effect, the ideal stiffness k can be obtained if the coefficient of sliding friction is known as well. However, this is not typically the case. Boundary conditions are an important concept for this research and are discussed in Chapter 4.

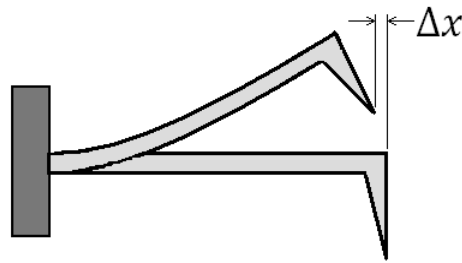


Figure 1-8. Foreshortening from vertical bending.

Traceability

Proper calibration of stiffness should follow a clear path of traceability to the Système International d'Unités (SI). Traceability is the chain of calibrations that link any sensor/instrument through a direct path, with defensible uncertainty statements for each measurement, to a primary standard. This primary standard, which reflects a physical realization of the unit of measure, is defined and maintained (if necessary) by national measurement institutes (NMIs). Traceability enables measurement uncertainty to propagate through the chain of calibrations and thus identifies the uncertainty for measurements performed by a given sensor or instrument. This notion of standardized units and measures allows quantitative data to be compared between organizations, manufacturers, and laboratories, facilitating collaboration and reproducibility of results. Traceability is sometimes difficult to obtain depending on the calibration technique.

Therefore, the approach adopted by the National Institute of Standards and Technology (the national measuring institute for the US) has been stiffness transfer by cantilever artifacts. This technique has been traceably compared to the geometrical model as well as the popular thermal calibration technique [11] and agreement within ~5% has been obtained [4].

The Force Equation

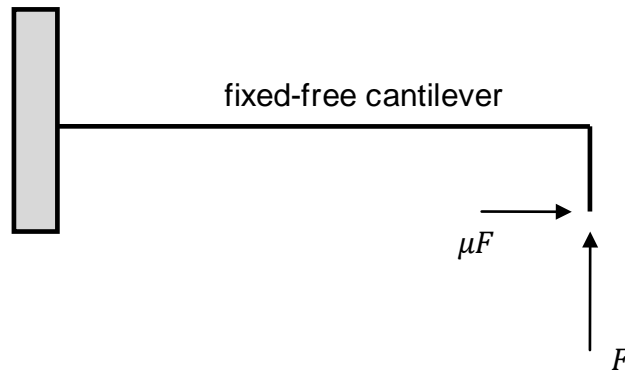


Figure 1-9. Cantilever with a friction force proportional to the applied force, F .

As noted, the most popular approach for AFM force measurement is to apply Hooke's law, $F=ky$. The choice of this equation stems from the single point detection scheme used to monitor the cantilever deformation. With only a single point of displacement, the force transduction constant must be stiffness (N/m). The general Euler-Bernoulli beam equation relating a beam's deflection to the applied load is,

$$\frac{\partial^2}{\partial x^2} \left(EI \frac{\partial^2 y}{\partial x^2} \right) = u \quad (1-5)$$

where x is the distance along the beam axis, y is the deformation perpendicular to the beam axis, I is the second moment of area, and u is a distributed load. Four integrations are necessary to obtain the force-displacement equation, which requires four boundary conditions. Because the moment boundary condition is impossible to know without

detailed knowledge of the contact mechanics, the challenge of force measurement by AFM can be summarized as attempting to solve an underdetermined equation.

As an exercise, the beam equation is solved assuming friction proportional to the applied force at the tip in order to illustrate how $F=ky$ can be replaced with an improved force-displacement relationship (Figure 1-9). Assuming $y=y(x)$, $u=0$, and EI is constant, integration is straightforward ($EI d^4y/dx^4=0$) and yields four equations,

$$EI \frac{d^3y}{dx^3} = \overset{-F}{\tilde{C}_1} \quad (1-6)$$

$$EI \frac{d^2y}{dx^2} = C_1x + C_2 = M \quad (1-7)$$

$$EI \frac{dy}{dx} = C_1 \frac{x^2}{2} + C_2x + \overset{=0}{\tilde{C}_3} \quad (1-8)$$

$$EIy = C_1 \frac{x^3}{6} + C_2 \frac{x^2}{2} + C_3x + \overset{=0}{\tilde{C}_4} \quad (1-9)$$

where C_{3-4} are zero due to the fixed base boundary condition (zero motion and slope at the base), C_1 is equal to the perpendicular force component (by force balance with shear force), and Equation 1-7 is equal to the bending moment M along the beam. The bending moment equation captures the friction contact mechanics and is,

$$M = F(L - x) + \mu Fr \quad (1-10)$$

where μ is the coefficient of sliding friction and r is the tip (stylus) height. The resulting deflection equations for any point on the beam and for the tip location ($x=L$) are,

$$y(x) = \frac{F}{6EI} (3Lx^2 - x^3) + \frac{\mu Fr}{2EI} x^2$$

$$y(L) = \frac{FL^3}{3EI} \left(1 + \mu \frac{3r}{2L} \right) = F \underbrace{\left[\frac{1 + \frac{3r}{2L}\mu}{k} \right]}_{\text{system compliance}} \quad (1-11)$$

The addition of friction makes the force equation more complex than $F=ky$. In practice, this friction analysis is too simple. Under the assumption that macroscopic friction

applies to the atomically sharp stylus, there must be static friction as well. Unlike kinetic friction, static friction is not a proportional relationship to normal force except at its maximum. Therefore, measurements performed where there is no sliding (such as part of stick-slip events) include an unknown quantity in the final displacement equation,

$$y(x) = \frac{F}{6EI}(3Lx^2 - x^3) + \frac{\overset{G_{max}=\mu_{static}F}{-G_{max}\leq G\leq G_{max}}}{2EI}rx^2 \quad (1-12)$$

where G is the friction resisting sliding. Simplifying to the tip location ($x=L$) does not give a clear relationship between the applied force F and the tip motion $y(L)$. When the macroscopic friction model is insufficiently accurate or when other forces contribute, such as electrostatic, osmotic, and/or magnetic forces, this entire analysis is invalid. Ambiguities like this will always exist in the force equation if a force relationship is unknown *a priori*, which is true in virtually every measurement situation. This makes exploratory force measurements particularly difficult since the environment has yet to be characterized. Therefore, a new force measurement paradigm is necessary to move toward more accurate force metrology.

CHAPTER 2 LITERATURE REVIEW

Historical Development

The atomic force microscope was introduced by Binnig, *et al.*, in 1986 to measure micro-scale forces [12]. Just prior to the invention of the AFM, the scanning tunneling microscope (STM) [13] was developed. This was a surface profilometer which used the strong variation in electron tunneling current with separation distance to map a sample surface. It only worked on conductive samples. The AFM was developed to expand the types of surfaces that could be probed. The idea was to use a compliant structure with a sharp tip that, when probing a surface, would deform from forces applied to the tip. Since all materials generate reaction forces to the probe's applied pressure, the AFM was not limited to imaging conductive materials. More importantly, force could be inferred from the deformation of the compliant structure. Initially, a simple rectangular cantilever was utilized as the compliant structure and a scanning tunneling microscope was used as the cantilever displacement sensor.

Since 1986, the AFM cantilever has been adapted to suit a wide range of applications. For example, two-arm triangular cantilevers increase the torsional rigidity and reduce the sensitivity to torsional loads. Coating the cantilever surface with thin films has become a standard method to increase detector sensitivity, enable biological imaging, and/or make the cantilever conductive. Additionally, various tip geometries such as spheres and carbon nanotubes are applied. Self-actuating piezoelectric cantilevers are used in cantilever arrays which enable a large sample area to be imaged rapidly. Since cantilevers are interchangeable, they are specialized to suit the specific environment. Therefore, no one design is used exclusively of the others.

The displacement detector has also taken several forms. A capacitive sensor over a double leaf cantilever was developed [14]. Heterodyne and homodyne interferometry have been used with different laser sources such as He-Ne lasers and laser diodes [15,16,17,18]. Additionally, heterodyne interferometry applied over a small spot on the cantilever enabled the 3D surface under the spot to be visualized [19]. Torsion of the cantilever was detected with this approach. A laser was used in the optical lever technique [20] and torsion could be detected depending on the photodiode arrangement. Finally, the cantilever itself has been used as the detector through the piezoresistive effect [21]. Each detector scheme has situational advantages, but the most broadly adopted scheme used today is the optical lever technique. Since the detector is not interchangeable, most commercially-available systems rely solely on this technique.

Applications of the Atomic Force Microscope

AFM has become ubiquitous in the research setting. Since the AFM can image non-conducting samples, it is commonly used in ultramicroscopy (imaging at atomic resolutions). For example, the AFM is used in biological [22], crystalline growth [23], and pharmaceutical drug [24] imaging applications. However, the AFM is not restricted to imaging. It is also used in atomic scale manipulation [25], such as nanolithography [26], and data storage and retrieval, such as IBM's Millipede project [27]. The AFM has also become a potential tool for quality control in microelectromechanical systems (MEMS) as a parallel to electronic quality control in microchip manufacturing [28]. This is due to the AFM's force measuring capabilities, which enable material and mechanical testing. Many fields can take advantage of the AFM's ability to measure micro-scale forces. For example, the structure of DNA is known, so current efforts are directed at measuring the

bonding forces between complementary nucleotides [29]. The mechanical stability of proteins has also been tested [30]. In surface science, the AFM is applied to friction measurements, such as between microspheres [31] and in capillary force analysis [32].

Force Modeling

Force is computed through its relationship to the cantilever's deformation. This relationship, called the force model, is based on Hooke's Law which is an integral part of linear elastic theory. Hooke's law provides a constitutive equation that relates stress with strain (force, F , with displacement, y). Since the detector in AFM measures displacement, Hooke's law is applied directly as $F=ky$. This displacement relationship is the most common force model for AFM [9]. However, it has been recognized that this model is too simplistic. Other force models have been proposed which take into account forces that arise from contact mechanics at the cantilever's tip. These have attempted to capture tip geometry [33], elastic deformation of the sample [34], cantilever inclination angle [5], adhesion [35], and friction [36,37]. Many times the model is situational. For example, if the sample is very hard, plastic deformation is unlikely to occur or, if the cantilever and sample are submerged in water, capillary force is mitigated. Therefore, it is necessary to understand the test environment in order to choose a model and determine its parameters.

Calibration

The AFM system must be calibrated to obtain reasonable measurement accuracy. The literature focuses heavily on stiffness calibrations because stiffness is the most difficult parameter in the force equation to calibrate. Calibration may be divided into four categories: dimensional, intrinsic, dynamic, and static.

Dimensional methods use estimations of the geometrical parameters of the cantilever and beam theory to predict stiffness. Computations may be carried out analytically or via finite element analysis. Relevant parameters include length, thickness, width, film thickness, modulus of elasticity, and second moment of area. Depending on the method, compensation can be made for V-shaped beams (double arm cantilevers) [38] and the trapezoidal cross-section seen in some commercial cantilevers [39]. Accuracy is limited by the combined standard uncertainty from each measurement; thickness, length, and Young's modulus are typically the largest error contributors.

Intrinsic methods attempt to apply naturally occurring phenomena. An example is force measurement on DNA [40]. Since the bonding energy of DNA is specific and highly reproducible, the force to pull DNA apart is reproducible. Such artifacts are nearly identical in nature and can be mass-produced by the millions. A critical parameter for such a calibration is temperature since, in general, increasing temperature reduces the additional energy required to rupture bonds.

Dynamic methods use cantilever vibration to estimate stiffness from frequency shift or phase change. One of the first techniques that applied this dynamic approach was developed by Cleveland *et al.* [41]. In this technique, a known mass was attached to the end of the cantilever and the corresponding reduction in natural frequency was measured. The location of the mass on the beam is a critical parameter and removing the mass after calibration is not trivial. Mass has also been added using different materials such as thin gold films [42], water droplets dispensed from an inkjet [43], and even other cantilevers [44]. Other researchers altered the method so that mass addition

was not required. A well-known method proposed by Sader *et al.* [45] uses the resonant frequency together with the Q (damping) factor in a fluid, usually air. The use of fluid dynamics has become more common, especially in colloidal probe microscopy, because the cantilever has a sphere for a tip and spheres are convenient to model in fluid dynamics [46]. Another approach uses the equipartition theorem and thermal oscillations of the cantilever to determine cantilever stiffness [47]. With corrections made for the laser spot size [48] (a laser is used to determine cantilever deflection), this method has become popular due to its application ease.

Static methods involve applying known forces directly to the cantilever and observing the resulting deflection. They are the most direct measurement of cantilever stiffness. Many devices have been used to apply a direct force to the cantilever. These include macro-sized (“relatively large”) cantilevers [49], piezoresistive levers [50, 51], and nanoindentation machines [52]. The measurement uncertainty in these experiments has been as high as 20%. The most sensitive parameter is claimed to be the load application point. Since the stiffness is related to length by an inverse cube law, small changes to load application point result in large errors in stiffness. To address this issue, Cumpson *et al.* [53-55] at the National Physics Laboratory, Teddington Middlesex, UK, have developed a series of micromachined artifacts for cantilever calibration. These artifacts have fiducials for locating the load application point and are available in a variety of shapes to accommodate a wide stiffness range. Some even include a built-in mechanism for calibrating themselves [56]. Gates *et al.* developed arrays of reference cantilevers with sufficient fabrication repeatability that a calibration performed on a single cantilever is representative of the entire array [57].

There are also additional calibration challenges. The stiffness has been shown to change in response to wear at the tip [33] and over time even if unused [2]. Given the difficulties associated with stiffness calibration and force model development, this research introduces a new measurement paradigm. Instead of a single point measurement of the tip displacement, the full-field displacement of the 3D surface of the cantilever is obtained.

CHAPTER 3 THREE-DIMENSIONAL IMAGING

A New Platform

Three-dimensional imaging requires a platform different from traditional AFM. This chapter discusses the design of the prototype platform used in this study and presents its capabilities and restrictions. The platform consists of a scanning white light interferometer (SWLI), holders for the cantilevers, a translation stage, a rotation (tip-tilt) stage, and an adapter plate to connect these units to the SWLI table (Figure 3-1).

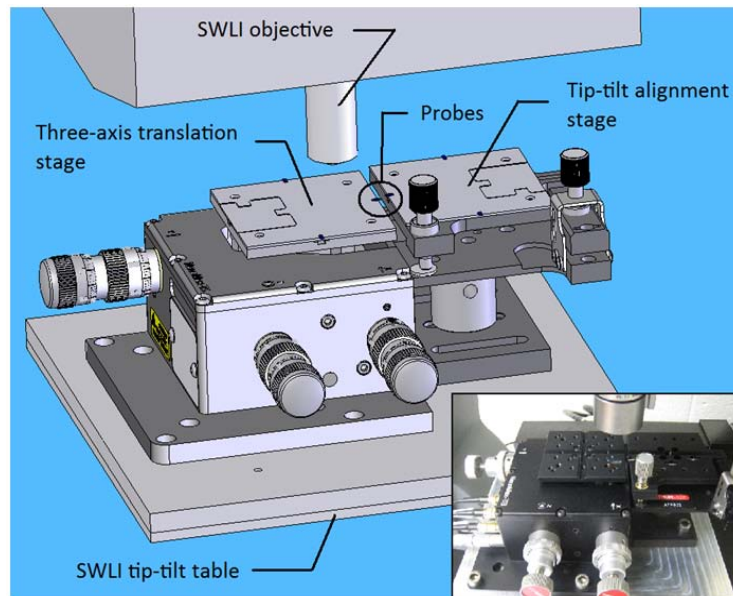


Figure 3-1. Prototype platform assembly. It is composed of a scanning white light interferometer (SWLI), a translational stage, and a tip-tilt stage.

Scanning White Light Interferometer

A key platform component is the SWLI, an optical 3D surface profiler that uses interference of a broad spectrum light source, or “white light”, to measure surface topography (Figure 3-2). Light reflected from the sample interferes with light reflected from a reference surface, but unlike coherent source interference, the white light interference only occurs over a small optical path difference. By translating the objective

(which carries the reference surface) relative to the sample, a plot of the interference intensity for this path difference range can be captured on a pixel-by-pixel basis by the SWLI detector. The location of the modulated intensity region (due to the alternating constructive/destructive interference) indicates the relative height of the sample at that pixel. Each pixel on the detector corresponds to a lateral position on the sample; the field of view for the corresponding height map depends on the system magnification. A Zygo NewView 7200 was used in this research. The selected system included a motorized translation/rotation (or X/Y/tip/tilt) table for sample alignment to the optical axis. As shown in Figure 3-1, the prototype platform is mounted to this table.

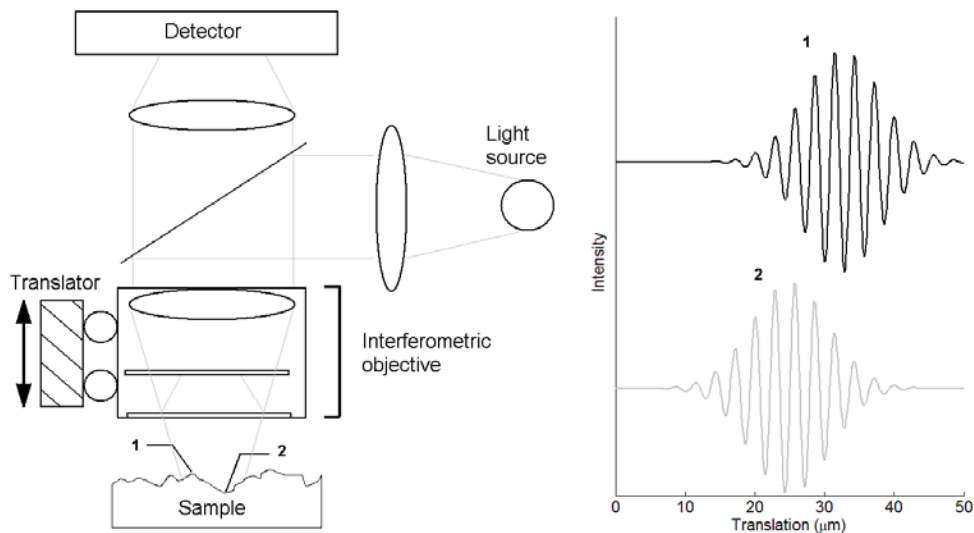


Figure 3-2. SWLI schematic. A Mirau objective is represented, although other types are available. The left-to-right offset between the interference intensity from positions 1 and 2 indicates their relative height difference (positive translation in the upward direction).

There are constraints associated with SWLI measurements. First, a full height map takes several seconds to acquire, in general, since the objective must be translated. During this time the sample dynamics must be interrupted (this pseudo-static approach is applied in this study) or synchronized with the measurement (this strobing approach

is not used here). Second, the lateral resolution is typically orders of magnitude coarser than the vertical resolution along the optical axis. For the experiments reported here, two objectives were used: a 5x Michelson with a lateral resolution of 2.2 $\mu\text{m}/\text{pixel}$ and a 20x Mirau with a 0.55 $\mu\text{m}/\text{pixel}$ lateral resolution (1x zoom and 640x480 pixel detector). In comparison, the NewView 7200 literature specifies a vertical resolution of 0.1 nm, although this value is dependent on the noise floor imposed by the measurement environment. Therefore, tests were performed to determine the repeatability for the experimental setup. A smooth silicon surface was placed on the stage at the cantilever loading location and 130 scans were completed using a 40 μm vertical scan range. The height repeatability for each pixel was then assessed. It was found that, on average, each pixel reported the same position within a standard deviation of 2.7 nm. Therefore, a resolution of 2.7 nm was assumed. Third, the SWLI cannot detect large changes between adjacent points, so there is a maximum slope that can be detected. This slope varies depending on the selected objective/zoom; it was 4 deg for the 5x objective and 18 deg for the 20x objective (each at 1x zoom).

Cantilever Holders

Aluminum plates with dimensions of 60 mm x 60 mm x 3 mm were fixed to the stages (Figure 3-3). Cantilevers and test surfaces were adhered to the plates at the midpoint of three sides (a fourth side with a specialized geometry was also available to enable cantilever alignment in future work). This design allowed the holder to be unscrewed and rotated to select the next cantilever for experimentation while approximately maintaining the same position in the SWLI field of view. A similar configuration was used for tests with a cantilever contacting a rigid surface. Cantilevers

and rigid surfaces were bonded to the holders with adhesive to enable the required top-down view for the SWLI measurements.

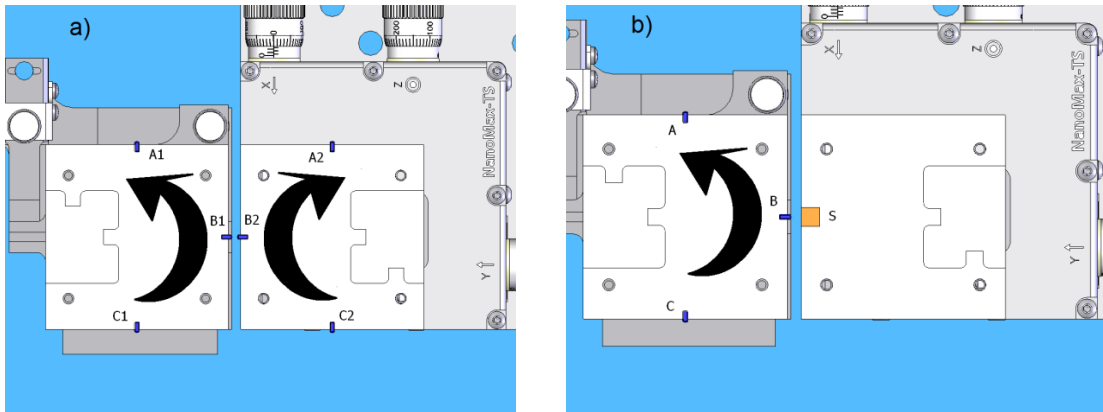


Figure 3-3. Example cantilever placement on the aluminum holders (top views). The individual cantilevers are too small to be seen at this scale, but the monolithic base chips are labeled A1-C2 (a) , A-C (b), and a rigid sample is labeled S (b). If the holders were unscrewed and rotated in the indicated direction, the next experiment would be C1 against C2 (a) and C against S (b).

Stages

The positioning stage (Thorlabs MAX301) was a three-axis, parallel kinematics, flexure based design with 4 mm of coarse motion (thumbscrew actuation) and 20 μm of fine motion driven by piezoelectric actuators with strain gauge feedback. The motion was controlled by a Thorlabs BPC103 controller. The second stage was a manual tip-tilt platform (Thorlabs ATP002) positioned on a base assembly (Thorlabs AMA501) which enabled equal height, side-by-side use with the positioning stage. The tip-tilt platform provided ± 4 deg of roll and pitch and acted as the fixed stage in the experiments. Any cantilever on this stage could be tilted into alignment with the positioning stage and then held fixed for the duration of the experiment.

The positioning stage's vertical linearity was tested from 7 μm to 20 μm within the 0-20 μm range of the piezoactuators. A silicon surface was adhered to the holder on the positioning stage. A second silicon surface was adhered to the holder on the tip/tilt

stage. The SWLI was used to measure the height difference between the two surfaces as the positioning stage was translated along the optical axis using 1 μm increments. The result (Figure 3-4) reveals a scale error of 79 nm/ μm . Though this quantity was available, the experimental results performed in this study did not require motion of the positioning stage, i.e., only features within the SWLI scan range were used, so this scale factor was not required in the data analysis.

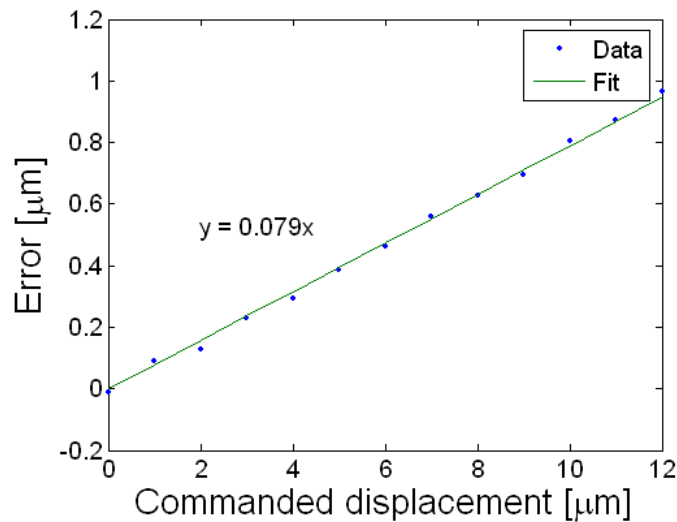


Figure 3-4. Positioning stage scale error. This was determined by comparing stage vertical position to displacement determined from SWLI measurement.

Platform Assembly

The platform assembly rested on the SWLI motorized table. During use, the platform positioning stage was first aligned to the SWLI optical axis using the table. Then, the tip-tilt stage was aligned to the positioning stage. Since the SWLI angular detection limit can be low (depending on the objective and effective magnification), proper alignment is important to maximize the available measurement range. Additionally, aligning to the optical axis ensures that the vertical motion from the positioning stage produces no lateral motion in the field of view.

Visualization of Quasi-static Bending

The prototype platform enables the direct visualization of cantilever deformations without the need for interpretation via a single point measurement of the cantilever tip motion used in conjunction with beam models. In this section, cantilever deflection measurements are provided. Various loading conditions are represented including no loading, rigid surface loading, and cantilever-on-cantilever loading. The results are discussed and the primary imaging limitations noted [58].

Residual Stress, “Batwings”, and Differencing

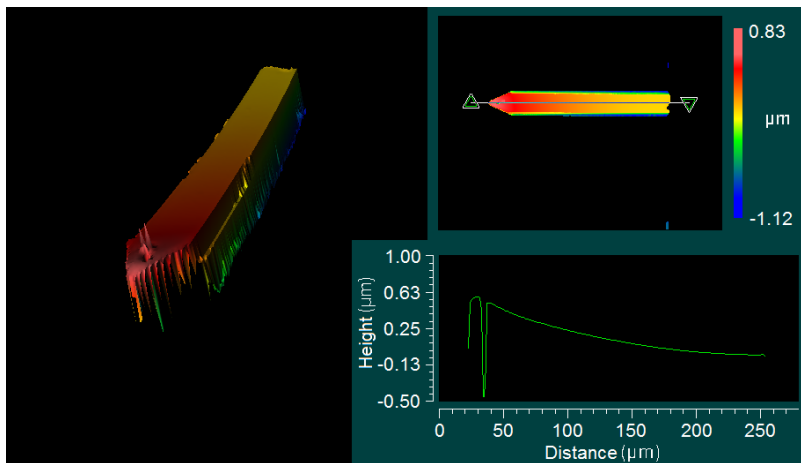


Figure 3-5. The Olympus OMCL-AC240TS cantilever. The deformed shape has approximately $0.5 \mu\text{m}$ of initial tip deflection.

The cantilevers presented here had a non-planar shape even in the absence of an external load. Cantilevers are typically designed to be flat, but residual stresses from the surface coating often lead to unwanted deformation. This deformation is typically small, but is observable in the SWLI measurements. Figure 3-5 shows the reflective backside of an Olympus OMCL-AC240TS (1.8 N/m stiffness) cantilever (i.e., the side the laser would normally reflect from in an AFM). It is seen that the cantilever deformation is approximately $0.5 \mu\text{m}$ at the tip with no external load applied. An imaging artifact

sometimes referred to as “batwings” is also observed. These spikes along the periphery of the cantilever are false height readings and tend to occur at steep height transitions. The speck near the tip (also visible in the section view) is surface contamination and also causes the bat wing effect. Additional cantilever measurements are shown in Figure 3-6. The data were collected using a 20x objective at 1x zoom in the 320x240 pixel mode.

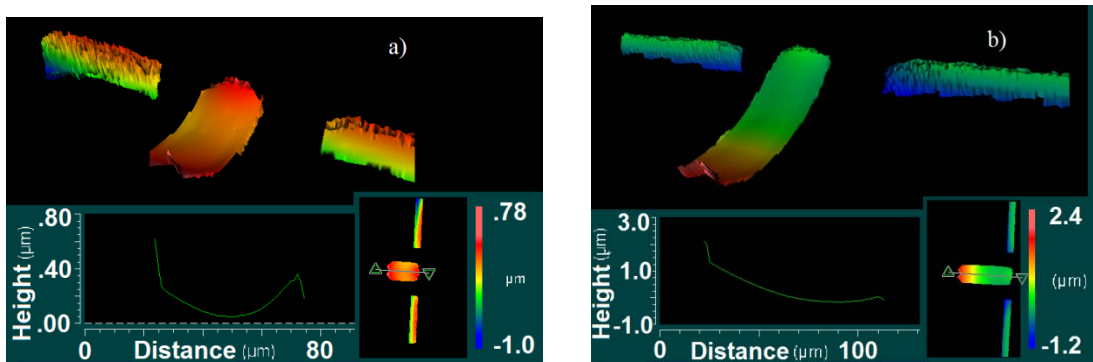


Figure 3-6. Olympus BL-RC150VB AB cantilevers. Stiffness is 0.03 N/m (a) and 0.006 N/m (b). The deformation levels are $\sim 0.25 \mu\text{m}$ (a) and $\sim 1 \mu\text{m}$ (b) in the absence of external loads.

When studying deformation of beams it is necessary to separate the contribution due to the external force(s) from those caused by other sources such as residual stress. For linear elastic beam models, deformation follows the rule of superposition. Therefore, in each of the analysis results presented here, the cantilever was measured before applying external loads. This reference image was then subtracted from all subsequent images to isolate the relative deformation caused by the applied forces. This differencing does not remove the bat wings, however, as these locations tend to report random erroneous heights from image to image.

Snap-in

When an AFM cantilever is placed in close proximity to a surface, an attractive force develops which pulls the tip closer to the surface. At a critical gap size, the attractive force overcomes the cantilever's restorative elastic force and the tip snaps into contact with the surface. This attractive force represents one of the many forces an AFM cantilever experiences. Snap-in behavior was measured for an Olympus OMCL-AC240TS (1.8 N/m) cantilever positioned near a smooth silicon surface (Figure 3-7). For these measurements, the silicon surface was mounted on the three-axis positioning stage and moved toward the cantilever in 50 nm steps. The sequence of three plots included in Figure 3-7 displays the cantilever deformation profile for three stage locations. In position 1, the silicon surface is sufficiently far from the cantilever so that no appreciable attractive force is present. In position 2, snap-in has occurred. The cantilever deflection is approximately 0.1 μm at the tip. In position 3, the stage has continued to move vertically past the cantilever's undeformed position so that it is deflected upwards. In Figure 3-7b, the centerline cantilever profiles are provided for the same three stage locations. The tip deflection versus stage motion is provided in Figure 3-7c; measurement points are identified by the small circles in 50 nm increments and the three locations from Figures 3-7a and 3-7b are presented by the large circles. Note that the information in Figure 3-7c is all that is available from standard AFM single point deflection metrology. All images were captured using a 20x objective at 1x zoom in 320x240 pixel mode. The SWLI data was differenced to isolate the deformation caused by snap-in and it was filtered to remove the bat wing artifacts.

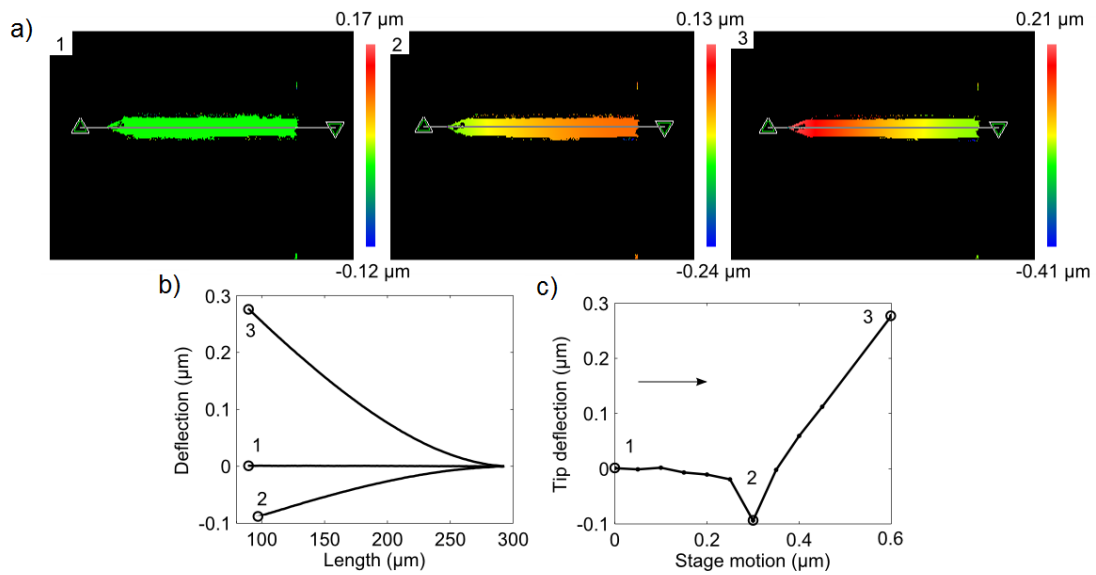


Figure 3-7. Cantilever snap-in demonstration. a) Height map of the cantilever at various stage locations, 1-3; b) corresponding two-dimensional profiles, 1-3; and c) traditional plot of stage motion versus tip deflection with 1-3 labeled. The arrow indicates the sequence of commanded stage motions.

Other Experiments

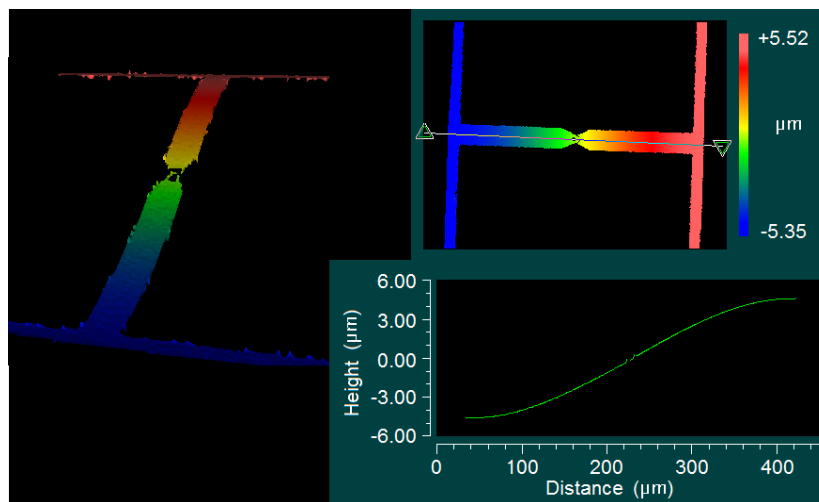


Figure 3-8. Two Veeco 1930 (1.3 N/m, 35 μm wide) cantilevers in contact. The left cantilever lever tip is positioned above the right cantilever lever tip.

One of the benefits of full-field imaging is the ability to capture height maps of the cantilever and sample simultaneously. For example, in cantilever-on-cantilever experiments using an AFM, measurements can only be made for the instrumented

cantilever leaving the deflection of the other cantilever to be inferred. Using the prototype platform, both cantilevers can be viewed simultaneously. Figure 3-8 shows two Veeco 1930-00 (1.3 N/m, 35 μm wide) cantilevers with one cantilever pushed against the tip of the other. There is approximately 9 μm of vertical offset between their bases and both cantilevers exhibit approximately 4.5 μm of end deflection. The objective used was 20x, 0.8x zoom, in 640x480 pixel mode.

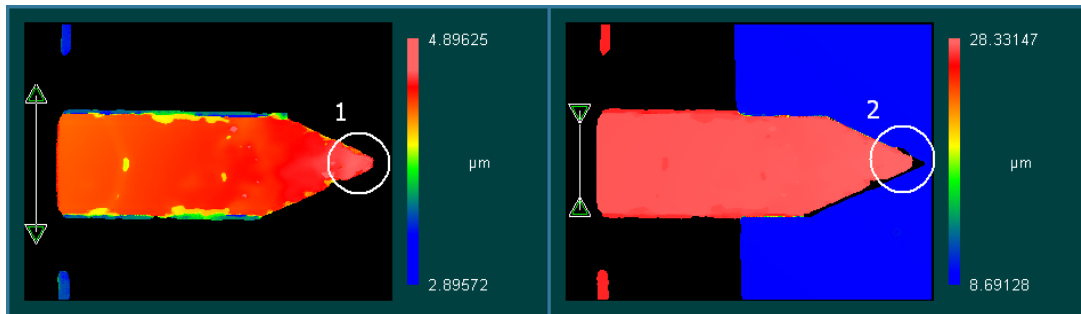


Figure 3-9. Data dropout. Due to SWLI measurement limitations this is commonly observed on the cantilever periphery (area 1 left image). This results in errors when determining the plan view dimensions. Including the sample in the measurement reveals lost data (area 2 right image).

The sample can also be used as an aid in SWLI measurements of a cantilever's plan view dimensions. Due to SWLI measurement limitations, data dropout is common at the cantilever periphery. However, by placing a smooth sample underneath the cantilever as a backdrop, the lost pixels can be revealed (Figure 3-9). Additionally, the sample can aid in tip wear analysis. Though not demonstrated here, it is feasible to measure the distance from the sample to the surface of the cantilever to estimate progressive tip wear as depicted in Figure 3-10.

Finally, an example of the platform's capability to identify anomalous bending behavior is presented in Figure 3-11. Here, an Olympus OMCL-AC160TS (42 N/m) cantilever was pressed against a smooth silicon surface. The deflection profile was

linear, rather than the expected cubic behavior. It is assumed that a crack at the cantilever base caused this hinge-like bending behavior. The cantilever broke off the base chip before this could be confirmed, but the fracture location supports the crack assumption. The imaging parameters included a 20x objective, 1x zoom, and 320x240 pixel mode.

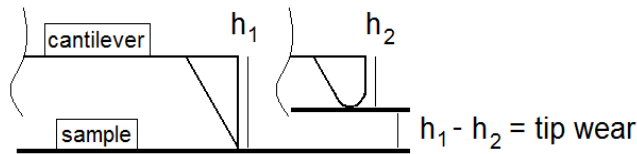


Figure 3-10. Tip wear estimation. Using SWLI measurements that include the sample surface in the view, an initial measurement, h_1 , can be compared to a current measurement, h_2 , to find the tip wear, $h_1 - h_2$.

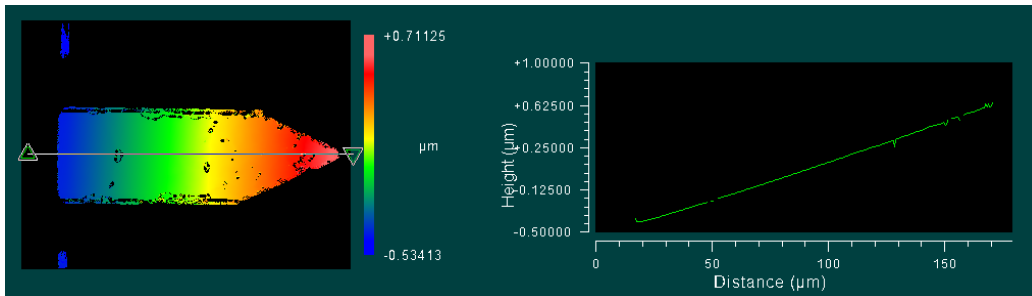


Figure 3-11. Anomalous bending behavior. This Olympus OMCL-AC160TS (42 N/m) cantilever shows a linear bending profile rather than the expected cubic behavior.

CHAPTER 4 THREE-DIMENSIONAL FORCE MODELING

The 3D deflection data provided by SWLI significantly increases the amount of information available to determine force. To illustrate the mathematical method, the “normal” force component is determined first. A horizontal rectangular beam is loaded through contact at the stylus (Figure 4-1). Forces both perpendicular, F , and parallel, P , to the beam axis develop where the relationship between the two forces is unknown (for example, a proportional friction model is not assumed). The deflection equation is determined from the Euler-Bernoulli beam model. Assuming $y=y(x)$, $u=0$, and EI is constant, four integrations of the beam equation ($EI d^4y/dx^4=u=0$) yields,

$$y(x) = \frac{-F}{6EI}x^3 + C_2x^2 + C_3x + C_4 \quad (4-1)$$

where C_1 is determined by force balance with the shear force and C_{2-4} are normally determined by applying boundary conditions. Rather than applying boundary conditions and condensing the deflection equation to $y(x=L)$ as in the single point measurement paradigm, the SWLI data provides $y(x)$ for $0 \leq x \leq L$ so the full deflection equation is utilized. Equation 4-1 is re-written as a general third-order polynomial,

$$y(x) = B_3x^3 + B_2x^2 + B_1x + B_0 \quad (4-2)$$

where B_{0-3} are the polynomial coefficients. These coefficients can be estimated by a least-squares fit to the 3D data. Therefore, the normal force component F is directly related to the third order polynomial coefficient B_3 ,

$$F = -6EIB_3 \quad (4-3)$$

The transduction coefficient ($-6EI$) has many advantages over stiffness. First, it is independent of the beam length, while stiffness has a sensitive relationship to beam

length (1:3 length:stiffness error for a rectangular cantilever). Second, the equation holds regardless of load application point (this avoids another 1:3 error rate). Similarly, the measurement location does not affect the estimate of B_3 so there is no error for detector misalignment. Third, the normal force is completely decoupled from other forces (immune to stylus contact effects).

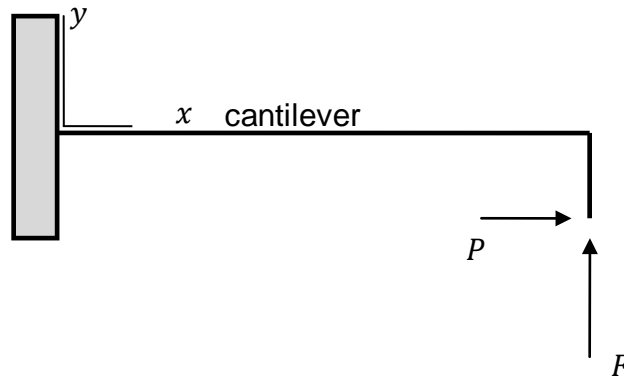


Figure 4-1. A cantilever loaded at the free end by two independent forces P and F .

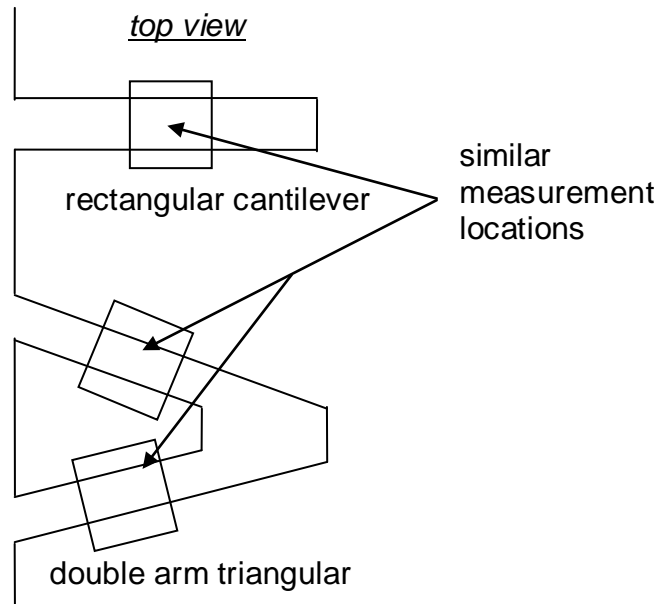


Figure 4-2. Force measurement does not depend on the global geometry of the cantilever. Both cantilevers shown utilize the same force equation except that the bottom cantilever should be measured on both arms (ideally each arm carries half the load).

The result is a direct application of the shear force equation for beams ($-EI d^3y/dx^3=V$). The shear force is constant along the length of the beam and is directly related to the third derivative of the beam deflection. This explains why the technique is independent of location along the beam and is independent of boundary conditions. Also, the entire beam does not have to be measured (though it improves the signal to noise ratio). Instead, a small section of the beam can be measured and, if the section is small enough (ideally, d^3y/dx^3 is infinitesimal), the shape change across the length of the beam is unimportant. This is in contrast to stiffness, which is dependent on the global shape of the beam to be solved analytically (shape is often restricted to prismatic beams). Therefore, many beam geometries are easily adapted to the 3D force technique, such as double arm triangular beams (Figure 4-2).

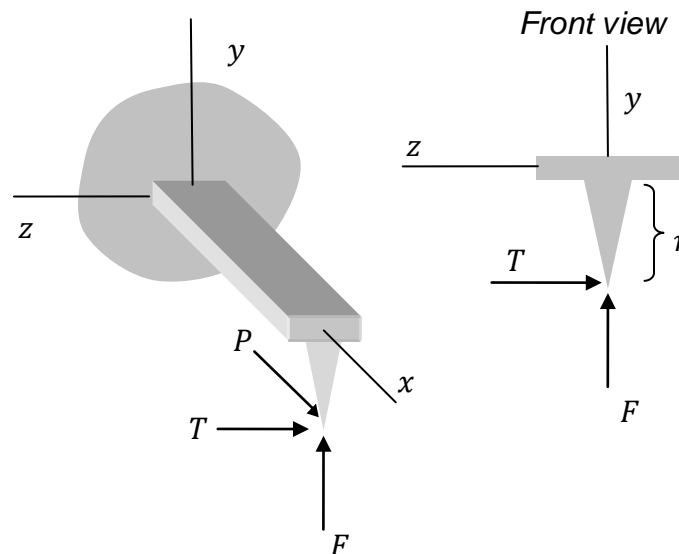


Figure 4-3. The 3D view of the forces acting on the cantilever.

A similar development yields expressions for the parallel force component, P , and torsional force component, T , to identify the full 3D force vector applied to the cantilever

$V(F, P, T)$, (Figure 4-3). First, the parallel force component, P , is derived. Using the same generic loading case in Figure 4-1, the moment equation is,

$$EI \frac{d^2y}{dx^2} = M = F(L - x) + Pr \quad (4-4)$$

where r is the tip height of the stylus. The deflection equation is then,

$$y(x) = \frac{-F}{6EI} x^3 + \left(\frac{FL}{2EI} - \frac{Pr}{2EI} \right) x^2 + \overset{=0}{\hat{C}_3} x + \overset{=0}{\hat{C}_4} \quad (4-5)$$

where C_{3-4} are zero for a fixed base boundary condition (motion and slope are zero) and C_2 is determined from the moment equation. Unlike shear, the moment depends on measurement location (not constant over the length of the beam). This is important when the location of the base and free end are not well known, which occurs when completing a SWLI measurement with a field of view smaller than the cantilever length. Here, the coordinate system of the measurement will not correspond to the coordinate system of the deflection equation which is centered at the base of the cantilever (Figure 4-4). Therefore, a polynomial fit to the deflection data cannot be used directly. Instead, the deflection equation is re-written for coordinate system independence so that a mapping can be performed between the polynomial fit of the data and the deflection equation. For example, both the deflection equation and polynomial fit can be mapped to,

$$y - y_0 = A_1(x - x_0)^3 + A_2(x - x_0) \quad (4-6)$$

where A_{1-2} are coordinate independent coefficients, and y_0 and x_0 translate the polynomial from the origin to an arbitrary coordinate system. Expanding the transform polynomial to relate to the deflection equation coefficients and polynomial fit coefficients yields,

$$y = \underbrace{\frac{-F}{6EI}}_{B_3} x^3 + \underbrace{\left(\frac{FL}{2EI} - \frac{Pr}{2EI}\right)}_{B_2} x^2 + \underbrace{(A_2 + 3A_1x_0^2)}_{B_1} x + \underbrace{(y_0 - A_1x_0^3 - A_2x_0)}_{B_0} \quad (4-7)$$

$$A_1 = B_3 = \frac{-F}{6EI} \quad (4-8)$$

$$A_2 = B_1 - \frac{B_2^2}{3B_3} = -2EI \frac{\left(\frac{FL}{2EI} - \frac{Pr}{2EI}\right)^2}{F} \quad (4-9)$$

Note that the A_1 coefficient does not vary with coordinate system, providing a second check on the invariance of measurement location for F . Solving for P in terms of the polynomial fit coefficients yields the measurement-independent result,

$$P = \frac{2EI}{r} \left[\sqrt{B_2^2 - 3B_3B_1 - 3B_3L} \right] \quad (4-10)$$

This result fully decouples P from the normal force F . However, determining P does require additional knowledge about the cantilever geometry, including tip height, r , and beam length, L . Note that beam length is not cubed and is therefore less sensitive to error than the single point approach.

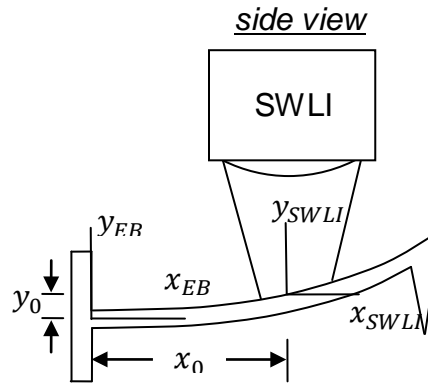


Figure 4-4. SWLI measurement coordinates. The SWLI has its own coordinate system (x_{SWLI}, y_{SWLI}) which is offset from the global coordinate system defined in the Euler-Bernoulli deflection equation (x_{EB}, y_{EB}) by an unknown amount (x_0, y_0)

The final force component, T , applies torsion to the beam causing twist. The twist equation can be derived using St. Venant's torsion theory which assumes the rate of

change of angular twist over the length of the beam, $d\alpha/dx$, is constant. The resulting equation for twist is,

$$\alpha = \frac{R}{GJ}x \quad (4-11)$$

where α is the angular twist, R is the applied torque, x is the position along the length of the beam, G is the material's shear modulus, and J is the torsion constant. Converting to deflection yields,

$$y(x, z) = \frac{R}{GJ}xz \quad (4-12)$$

where z is the location across the width of the beam. This equation assumes a particular coordinate system (origin at the base) so it can be generalized as,

$$y = \frac{R}{GJ}(x - x_0)(z - z_0) + y_0 \quad (4-13)$$

$$y = \underbrace{\frac{R}{GJ}}_D xz + \underbrace{\frac{-R}{GJ}x_0}_H z + \dots \quad (4-14)$$

A surface fit to the 3D data yields a coordinate-independent estimate of the coefficient D which is directly related to the applied torque,

$$\overset{Tr}{\vec{R}} = GJD \quad (4-15)$$

$$T = \frac{GJD}{r} \quad (4-16)$$

where T is the final force component of the 3D force vector applied to the tip.

CHAPTER 5
VALIDATION OF THE FORCE MODEL

Normal Loading

Equation 4-3 was evaluated for the case of a meso-scale horizontal beam (no tip) with a “normal” mass-based force applied (i.e., F was ideally the only force component). The beam was fabricated from a 50.8 mm diameter, double-sided polished <111> silicon wafer by diamond cutting at the flat. The design dimensions for the beam were 1 mm wide, 5 mm long, and 0.3 mm thick. After fabrication, the dimensions were measured using the SWLI. The average width was 0.941 mm and the length was 4.820 mm (the SWLI lateral resolution was 4.4 μm for a 5x objective at 0.5x zoom with a 640x480 detector). A thickness measurement was completed by placing a glass surface beneath the cantilever and using the SWLI to measure the distance from the top of the glass surface to the top of the cantilever. The thickness value, t , was 0.305 mm but varied depending on location by $\pm 9 \mu\text{m}$. A stitched SWLI image of the entire cantilever is shown in Figure 5-1.

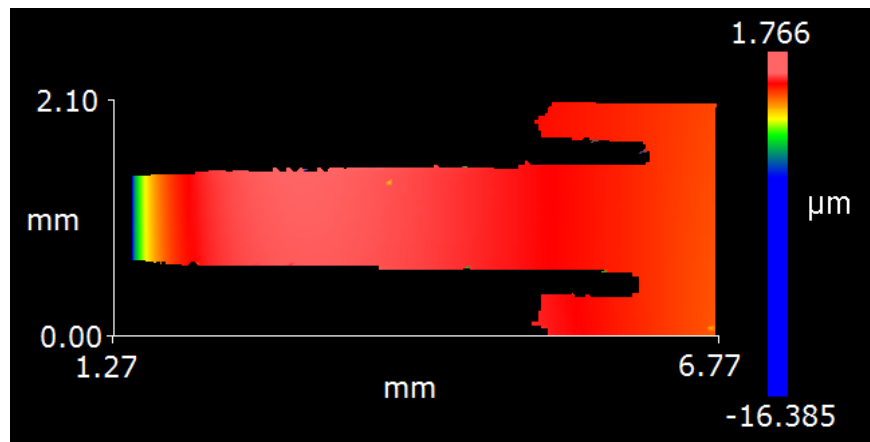


Figure 5-1. SWLI image of the fabricated cantilever. The enlarged field of view was enabled by stitching multiple images together. It is seen that the width of the beam varies slightly along its length. The wafer edge roll-off is observed at the free end (left end) of the beam.

The normal forces for the beam were produced using a series of 10 masses (Figure 5-2a); the individual masses were each suspended from a tether which was looped over the beam (Figure 5-2b). The mass values, m_{meas} , were measured using a Mettler Toledo AB265-S/FACT precision balance (0.1 mg resolution). The beam was fixed to a holder using Crystalbond™ heat-activated adhesive and the holder was bolted to the tip-tilt stage.

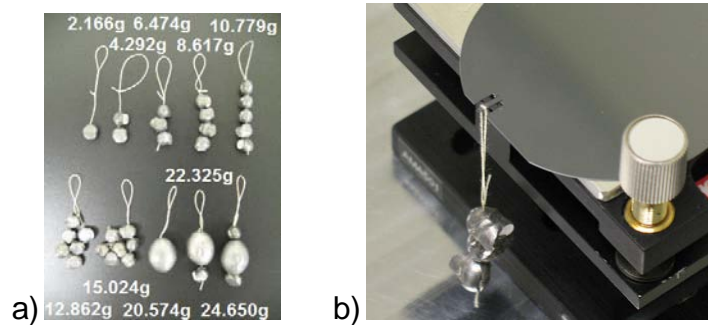


Figure 5-2. Fabricated masses. a) Masses used for vertical loading experiments, b) cantilever attached to the tip-tilt stage and loaded near the free end. Measurements are valid at any section between the base and the load point.

The measurement procedure was initiated by aligning the cantilever base to the SWLI optical axis (the optical axis was treated as parallel to the gravity vector, although the degree of alignment was not determined). To perform this alignment, a 5x objective with 0.5x zoom was applied to give a 2.82 mm by 2.12 mm field of view and 4.4 $\mu\text{m}/\text{pixel}$ lateral resolution. The cantilever was then laterally positioned under the objective using the motorized stage. The cantilever was longer than the field of view so only a section of the cantilever was measured; stitching was not applied for the force measurements. The following steps were completed for each mass.

- Attach the mass to the cantilever.
- Complete a first SWLI measurement.
- Remove the mass.
- Complete a second SWLI measurement.

The two SWLI measurements were differenced to isolate the deflection caused by loading. As described before, differencing isolates the deformation caused by the applied force from other sources. However, differencing requires lateral alignment between images. Therefore, the mass was applied first in the measurement sequence since it required the longest setup time. This reduced the time between steps 2 and 4 to a few seconds, which mitigated the effect of lateral drift due to stage settling and thermal effects. In addition to drift-related lateral motion, vertical deflection of the cantilever from an applied force also leads to a small shift (foreshortening) of the cantilever along the beam axis. Because the beam deflections were small in this study, this shear effect was neglected.

A deflection profile was obtained for each applied force by taking a section view through the beam center in the difference map (similar to the approach used for the AFM cantilevers shown in Figure 3-7). The section view data was then fit in a least-squares sense using a cubic polynomial to obtain the coefficient B_3 . Equation 4-3 was adjusted for $F=m_{est}g$ and divided by the measured mass m_{meas} to assist in the data analysis,

$$\frac{m_{est}}{m_{meas}} = \frac{-6E_{\langle 110 \rangle}IB_3/g}{m_{meas}} = 1 \quad (5-1)$$

where m_{meas} is the mass measured by the precision balance in kg, m_{est} is the mass estimated by the cantilever force equation in kg, $E_{\langle 110 \rangle}=168.9$ GPa [59], $I=wt^3/12$ for the rectangular cross-section, $t=0.305$ mm, and $g=9.81$ m/s². There was a noticeable taper in the width so the average value within the measurement field of view was used ($w=0.926$ mm). Equation 5-1 should equal 1 within the measurement uncertainty. The uncertainty was estimated from the uncertainties of each variable in Equation 5-1 and is

discussed later in the chapter. The results are displayed in Figure 5-3 with error bars based on the uncertainty analysis and multiplied by a coverage factor of 2. As seen in the figure, the estimated mass under predicts the measured mass by a mean of 9.6% but is within the error bars.

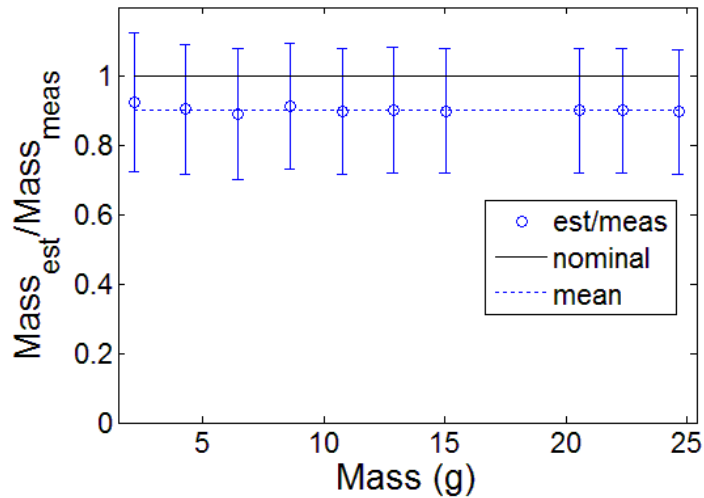


Figure 5-3. Results of Equation 5-1 for the 10 masses. The error bars are based on the full uncertainty analysis multiplied by a coverage factor of 2.

The variability of B_3 with profile location in a single measurement was also investigated. Eleven deflection profiles near the beam centerline were selected from a single image and used to individually calculate B_3 . The standard deviation was found to be 0.5% of the mean value. This deviation is an indicator of the model limits since the Euler-Bernoulli equations describe a two-dimensional beam. Noise in the SWLI height map from the single measurement result would also contribute.

Next, the cantilever was loaded and 11 separate measurements were sequentially completed before removing the load. Only the centerline profile was extracted from each measurement and was used to calculate B_3 . The standard deviation was found to

be 1.5% of the mean. This provides an indication of the limit imposed by the environmental noise over the required measurement time of approximately 4 minutes.

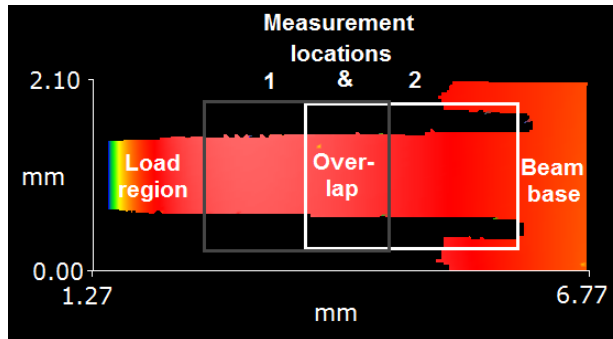


Figure 5-4. Beam loaded under identical conditions, but measurement field of view was varied. The boxes represent the partially overlapping measurement regions along the beam’s axis. For identical loading, the shear should be identical regardless of location.

Ideally, the force calculated using Equation 5-1 is independent of the measurement location for constant loading conditions. To test this behavior, a measurement (denoted 1) was completed for a field of view near the free end and compared to a measurement (denoted 2) completed near the base; see Figure 5-4. The values of B_3 differed, however, due to the tapering beam width (see Figure 5-1). To enable a direct comparison of the two results, it was necessary to consider the non-constant beam width and corresponding variation in the moment of inertia along the beam’s axis. This was accomplished using the average widths, w_{avg} , of the beam for the two selected fields of view. The result was evaluated by considering the ratio of the two measurement results 1 and 2 (same mass, but different location). After simplification, the ratio is,

$$\frac{(-6E_{<110>}IB_3)_1}{(-6E_{<110>}IB_3)_2} = \frac{\left(\frac{-6E_{<110>}w_{avg}t^3B_3}{12}\right)_1}{\left(\frac{-6E_{<110>}w_{avg}t^3B_3}{12}\right)_2} = \frac{(w_{avg}B_3)_1}{(w_{avg}B_3)_2} = 1 \quad (5-2)$$

which is nominally equal to 1. Experimentally, the ratio was determined to be 1.03 based on a mass load of $m=8.617$ g and the following values: $(B_3)_1=-37.02$ m⁻², $(w_{avg})_1=0.88$ mm, $(B_3)_2=-33.89$ m⁻², and $(w_{avg})_2=0.93$ mm. This deviation from unity is reasonable given the 1.5% standard deviation obtained from the repeated B_3 tests for a single load with the profile extracted along the beam's centerline.

In a second study of the polynomial fit-based force determination approach, a horizontal Olympus OMCL-AC240TS probe (rectangular cross-section, 30 μm x 2.8 μm, 240 μm length, $k=1.8$ N/m, approximately 14 μm tip height, less than 10 nm tip radius) was deflected vertically against a rigid, smooth silicon surface. The experimental B_3 value was -2.11×10^4 m⁻² from the centerline deflection profile. If the manufacturer-specified EI value of 8.29×10^{-12} N-m² is applied, the resulting vertical force is $F=-6B_3EI=-6(-2.11 \times 10^4)(8.29 \times 10^{-12})=1.05 \times 10^{-6}=1.05$ μN. Based on the measured deflection of 0.59 μm at the probe's free end (from the SWLI height map), the force obtained from the manufacturer's spring constant is $F=1.8(0.59 \times 10^{-6})=1.06 \times 10^{-6}=1.06$ μN. This gives a 1% agreement and provides a preliminary validation of the method for a typical AFM probe. Data was collected using a 20x objective, 1x zoom, 320x240 pixel detector.

In a final study, the full surface data of a cantilever was used to calculate the polynomial coefficients rather than taking a section view down the center of the cantilever axis. This was done in preparation for the torsion experiments which required the three-dimensional deformation data (see Equation 4-14). To accommodate a full surface fit, least-squares curve fitting was used again. The equation for the surface is a linear combination of each deformation,

$$y(x, z) = \underbrace{B_3x^3 + B_2x^2}_{\text{bending}} + \underbrace{C_1x + C_0}_{\substack{\text{bending} \\ \text{and} \\ \text{torsion}}} + \underbrace{Dxz + Hz}_{\text{torsion}} \quad (5-3)$$

Since the generic equations for bending and torsion contain both x and constant terms, these components are added together in Equation 5-3 and are represented by new coefficients C_1 and C_0 . For normal loading, the only component of interest was B_3 . Given a number of (x, z, y) points, Equation 5-3 can be written in matrix form,

$$\begin{bmatrix} x_1^3 & x_1^2 & x_1 & 1 & x_1z_1 & z_1 \\ \vdots & \vdots & \vdots & \vdots & \vdots & \vdots \\ x_n^3 & x_n^2 & x_n & 1 & x_nz_m & z_m \end{bmatrix}_{(n \times m) \times 6} \begin{Bmatrix} B_3 \\ B_2 \\ C_1 \\ C_0 \\ D \\ H \end{Bmatrix}_{6 \times 1} = \begin{Bmatrix} y_1 \\ \vdots \\ y_{n \times m} \end{Bmatrix}_{(n \times m) \times 1} \quad (5-4)$$

where m is the number of measurements across the width of the cantilever, n is the number of measurements down the length of the cantilever, and $m \times n$ is the total number of measurements. This can be compactly written as $[XZ]\{B\}=\{Y\}$ and solved for in the least squares sense using the pseudo-inverse,

$$\{B\} = [XZ]^+\{Y\} \quad (5-5)$$

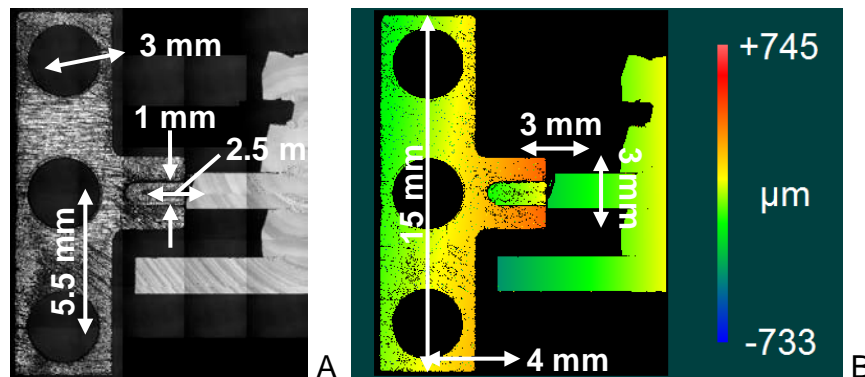


Figure 5-5. The aluminum “tee” bonded to a 1.5 mm wide cantilever. A) a microscope image of the tee, B) a SWLI height map of the tee. The images are stitched to enlarge the field of view. The groove near the cantilever is for alignment purposes.

A 1.46 mm wide by 0.311 mm thick by ~5 mm long cantilever was mass loaded to test this approach. Additionally, a removable “tee” was bonded to the cantilever to be used for the torsion experiments described later. The “tee”, shown in Figure 5-5, had three sockets to accept a stainless steel sphere which, in turn, held the masses. This configuration enabled repeatable positioning of the masses into the sockets. For normal loading, the center hole was used. Eight masses (3.260 g, 5.426 g, 7.552 g, 9.734 g, 11.877 g, 14.059 g, 16.122 g, and 18.285 g) were applied to the cantilever, with five trials per mass. The coefficients were determined using Equation 5-5 and the masses were computed using Equation 5-1. The results are shown in Figure 5-6 where the error bars are based on the uncertainty analysis and multiplied by a coverage factor of 2. The estimated mass under predicts the measured mass by a mean of 6.2% but is within the error bars.

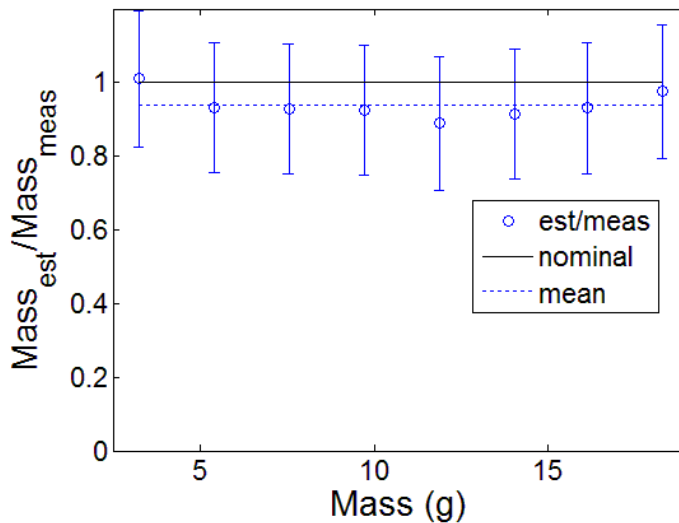


Figure 5-6. Results of Equation 5-1 for the 8 masses using the surface fit approach. The error bars are based on the full uncertainty analysis multiplied by a coverage factor of 2.

Torsion Loading

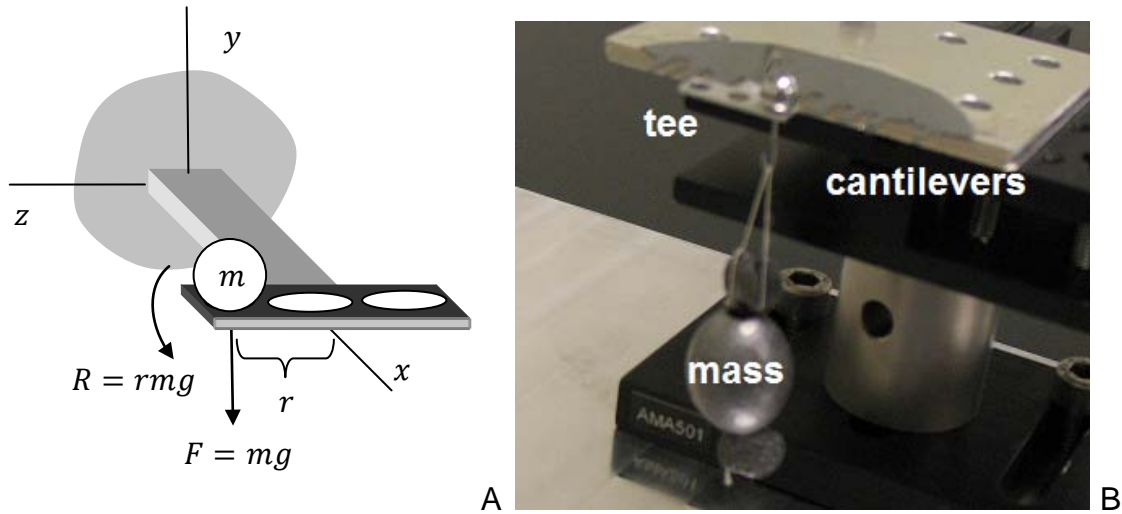


Figure 5-7. “Tee” attached to cantilever. A) Attaching a “tee” to the cantilever enabled offset loading, B) an array of cantilevers with one cantilever being loaded using the “tee”.

Equation 4-16 was evaluated on multiple cantilevers using offset loading as shown in Figure 5-7a. An aluminum “tee” was fabricated and bonded to the cantilevers (Figure 5-5). Three holes were drilled through the tee as load zones for a stainless steel sphere. The resulting ball and socket arrangement enabled precise placement of the sphere on the tee. A hook inserted through a hole in the sphere enabled it to support the masses. The tee was bonded to the free-end of the cantilevers using Crystalbond™ heat-activated adhesive. The assembly shown in Figure 5-7b enabled offset loading with a constant torque arm.

New cantilevers were fabricated with dimensions and torque arms shown in Table 5-1. Positive arms generated counter-clockwise twist and negative arms generated clockwise twist. The torque arm was defined as the perpendicular distance from the center of the hole to the cantilever beam axis. Since the tee was bonded manually, placement of the tee onto the cantilever was not tightly controlled resulting in cantilever-

to-cantilever variability in the torque arm alignment. Additionally, the field of view of the microscope was too small to simultaneously capture the holes and the cantilever in the same measurement and stitching was time intensive. Therefore, the torque arm was estimated based on the orientation of the alignment grooves to the cantilever axis and the known dimensions of the tee.

Table 5-1. Cantilever geometries. The thickness, t , was approximately 311 μm .

Cantilever number	Length (mm)	Width nominal (mm)	Width measured, w (mm)	Torsion multiplier, β [60]	Positive torque arm (mm)	Negative torque arm (mm)
1	5	1	0.959	0.263	5.339	NA
2	5	1.5	1.454	0.286	5.371	5.605
3	5	2.5	2.462	0.306	5.528	5.448
4	5	3	2.962	0.310	5.355	5.622
5	5	0.7	0.656	0.233	5.221	5.756
6	13	1.5	1.455	0.288	5.378	5.598
7	13	3	2.963	0.310	5.347	5.630
8	13	0.7	0.657	0.233	5.590	5.387

The cantilevers were each loaded with at least three different masses five times per mass in the same manner as for the normal loading experiments. The first mass was the smallest in the set (2.166 g). The third was the largest mass the cantilever could accept while still reflecting light back to the SWLI (note the SWLI has a maximum surface angle that it can measure which depends on the magnification). The other masses were selected to be between the first two. The coefficients were estimated using Equation 5-5 with the coefficient of interest being D . Equation 4-16 was adjusted to assist in data analysis similar to Equation 5-1,

$$\frac{m_{est}}{m_{meas}} = \frac{GJD/gr}{m_{meas}} = 1 \quad (5-6)$$

where m_{meas} is the mass measured by the precision balance in kg, m_{est} is the mass estimated from the cantilever force equation in kg, $54.0 \leq G \leq 64.7$ GPa depending on

width and thickness [61], $J=\beta wt^3$ (β and w are given in Table 5-1), $t=311 \mu\text{m}$, and r is the torque arm given in Table 5-1. The results for positive torque and negative torque are shown in Figures 5-8 and 5-9, respectively. The estimated mass under predicts the measured mass for positive torque loading by 7.4% and under predicts the measured mass for negative torque loading by 11.2%. The mean of the two results is 9.3%.

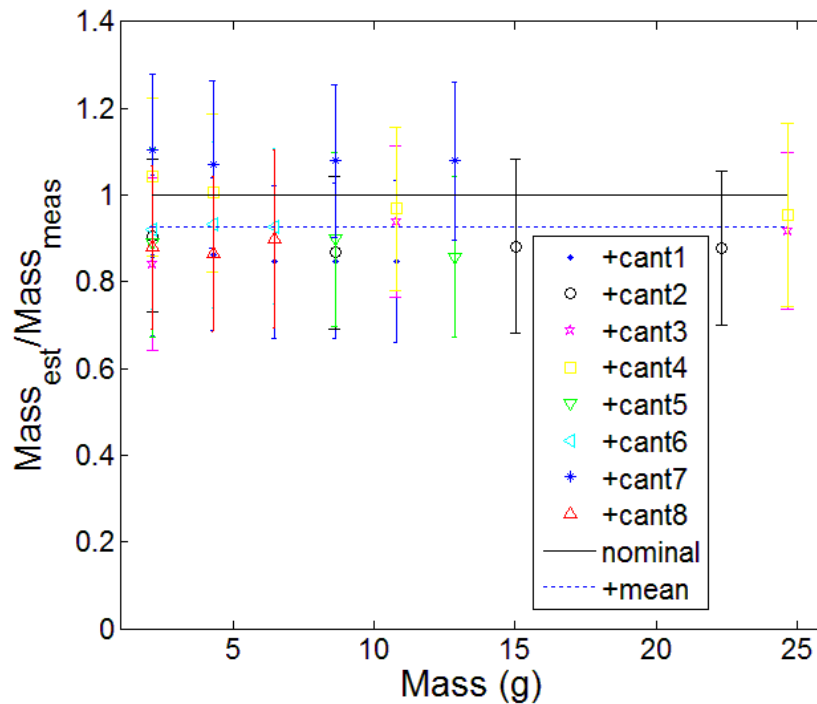


Figure 5-8. Torsion results when mass is loaded at the positive torque arm. The error bars are based on the full uncertainty analysis multiplied by a coverage factor of 2.

A second study was performed to determine if the normal and torsional components could be determined simultaneously with the same measurement. Figure 5-7a shows how an offset load produces both twist and bending deformation. Because the tee increased the effective length of the cantilevers, which subsequently increased the measurement sensitivity to external noise, two alterations to the setup were required to lower the noise levels. First, foam insulation was placed around the work area to

block air currents. Second, the tethers for the masses were replaced by a rigid, stainless steel link. Motion at the test mass was rigidly linked to the sphere which caused the sphere to rock in its socket and quickly damped vibrations.

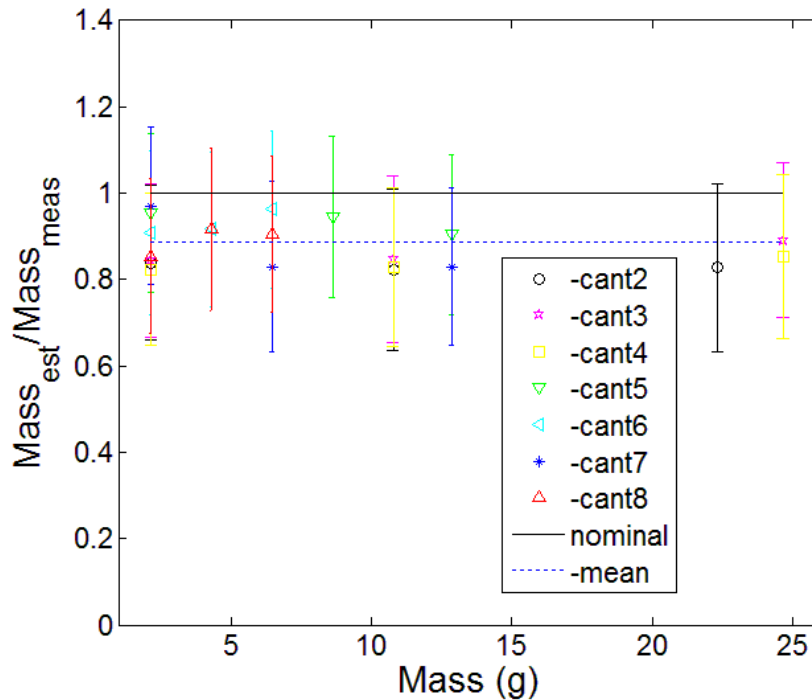


Figure 5-9. Torsion results when mass is loaded at the negative torque arm. The error bars are based on the full uncertainty analysis multiplied by a coverage factor of 2.

A 1.46 mm wide by 0.311 mm thick by ~5 mm long cantilever was used along with 5 masses (3.260 g, 5.426 g, 7.552 g, 16.122 g, and 18.285 g) applied at both positive and negative torque arms (5.464 mm and 5.515 mm respectively) with five trials per mass. The coefficients were determined using Equation 5-5, the mass estimated, and the results analyzed by Equation 5-6. Using the normal force coefficient yields the results shown in Figure 5-10 and using the torsion force coefficient yields the results shown in Figure 5-11 with the error bars based on the uncertainty analysis and multiplied by a coverage factor of 2. The mean estimated mass using the normal force

coefficient under predicts the measured mass by 8.0% and the mean estimated mass using the torsional force coefficient under predicts the measured mass by 11.9% (mean positive torque arm of 12.5% and mean negative torque arm of 11.2%).

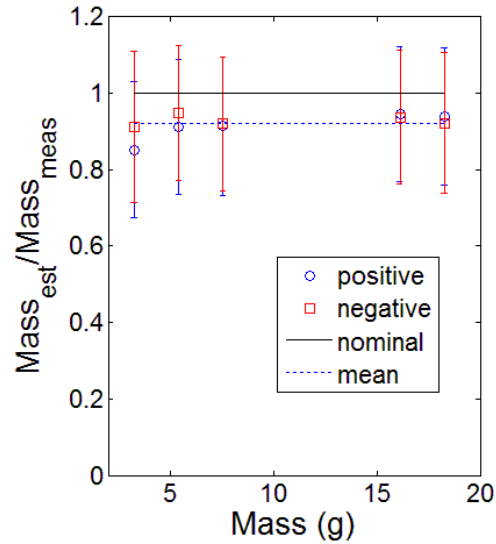


Figure 5-10. Torsion loading results for mass loaded at the positive and negative torque arms. The error bars are based on the full uncertainty analysis multiplied by a coverage factor of 2.

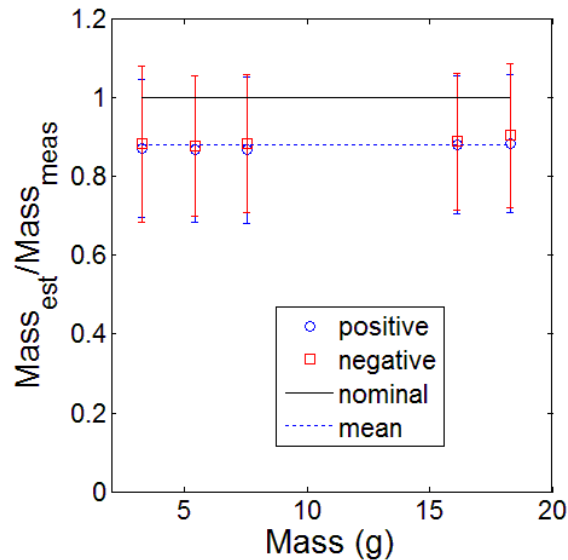


Figure 5-11. Normal loading results for mass loaded at the positive and negative torque arms. The error bars are based on the full uncertainty analysis multiplied by a coverage factor of 2.

Uncertainty Analysis

The measurement uncertainty reported in the figures was determined by the propagation of errors of Equations 5-1 and 5-6,

$$\left(\frac{\sigma_{m_{est}/m_{meas}}}{m_{est}/m_{meas}}\right)_{normal} = \sqrt{\left(\frac{\sigma_{E<110>}}{E<110>}\right)^2 + \left(\frac{\sigma_I}{I}\right)_*^2 + \left(\frac{\sigma_{B_3}}{B_3}\right)_*^2 + \left(\frac{\sigma_g}{g}\right)^2 + \left(\frac{\sigma_{m_{meas}}}{m_{meas}}\right)^2} \quad (5-7)$$

$$\left(\frac{\sigma_{m_{est}/m_{meas}}}{m_{est}/m_{meas}}\right)_{torsion} = \sqrt{\left(\frac{\sigma_G}{G}\right)^2 + \left(\frac{\sigma_J}{J}\right)_*^2 + \left(\frac{\sigma_D}{D}\right)_*^2 + \left(\frac{\sigma_g}{g}\right)^2 + \left(\frac{\sigma_r}{r}\right)_*^2 + \left(\frac{\sigma_{m_{meas}}}{m_{meas}}\right)^2} \quad (5-8)$$

where terms with asterisks can be expanded further. The terms I and J expand to,

$$\frac{\sigma_I}{I} = \frac{\sigma_J}{J} = \sqrt{\left(\frac{\sigma_w}{w}\right)^2 + \left(3\frac{\sigma_t}{t}\right)_*^2} \quad (5-9)$$

$$\frac{\sigma_t}{t} = \sqrt{\left(\frac{\sigma_t}{t}\right)_{resolution}^2 + \left(\frac{\sigma_t}{t}\right)_{standard\ dev}^2} \quad (5-10)$$

where w is the beam width, t is the beam thickness, “resolution” is associated with the SWLI height resolution, and “standard dev” is based on measurements of thickness at multiple locations on the beam. The terms B_3 and D expand to,

$$\frac{\sigma_{B_3}}{B_3} = \sqrt{\left(\frac{\sigma_{B_3}}{B_3}\right)_{least-squares}^2 + \left(\frac{\sigma_{B_3}}{B_3}\right)_{standard\ dev}^2} \quad (5-11)$$

$$\frac{\sigma_D}{D} = \sqrt{\left(\frac{\sigma_D}{D}\right)_{least-squares}^2 + \left(\frac{\sigma_D}{D}\right)_{standard\ dev}^2} \quad (5-12)$$

where the “least-squares” term is associated with the covariance matrix obtained during fitting and the “standard dev” term is based on the repeated trials of each mass load.

The term r , the torque arm, expands to,

$$\frac{\sigma_r}{r} = \sqrt{\left(\frac{\sigma_r}{r}\right)_{resolution}^2 + \left(\frac{\sigma_r}{r}\right)_{alignment}^2} \quad (5-13)$$

where “resolution” is associated with the SWLI lateral resolution and “alignment” is associated with the extrapolation of the hole location using the alignment grooves instead of a stitched image of the entire assembly. Representative values are provided in Table 5-2 where the largest uncertainty contributor, thickness (standard dev), is also the term that gets multiplied by three in Equation 5-9.

Table 5-2. Uncertainty contributions.

Name	Variable name	Value
Young’s modulus	$\sigma_{E_{\langle 110 \rangle}}/E_{\langle 110 \rangle}$	0.005
Shear modulus	σ_G/G	0.01
Cantilever width	σ_w/w	0.003-0.013
Cantilever thickness (resolution)	$(\sigma_t/t)_{resolution}$	1.7×10^{-5}
Cantilever thickness (standard dev)	$(\sigma_t/t)_{standard\ dev}$	0.029
Normal force coefficient (least-squares)	$(\sigma_{B_3}/B_3)_{least-squares}$	0.005
Normal force coefficient (standard dev)	$(\sigma_{B_3}/B_3)_{standard\ dev}$	0.02
Torsional force coefficient (least-squares)	$(\sigma_D/D)_{least-squares}$	0.0002
Torsional force coefficient (standard dev)	$(\sigma_D/D)_{standard\ dev}$	0.02
Gravity	σ_g/g	0.004
Torque arm (resolution)	$(\sigma_r/r)_{resolution}$	0.002
Torque arm (alignment)	$(\sigma_r/r)_{alignment}$	0.02
Mass measurement	$\sigma_{m_{meas}}/m_{meas}$	1.1×10^{-5} - 6.1×10^{-5}

Young's modulus for single crystal silicon depends on crystal orientation. For (111) silicon with the cantilever beam axis on the (111) plane, Young's modulus is independent of orientation with a value of 168.9 GPa. However, manufacturing limits prevent perfect alignment to the (111) plane. The manufacturer specified alignment tolerance to the (111) plane was ± 0.5 deg. Using the stiffness tensor for silicon and applying tensor rotations, the maximum error in modulus for wafer misalignment was determined to be 0.5% of 168.9 GPa.

A similar process was used to determine the uncertainty for shear modulus due to misalignment to the (111) plane. However, shear modulus does depend on the orientation of the beam axis on the (111) plane. The beam axis was nominally oriented along the $\langle -1-12 \rangle$ direction by cutting perpendicular to the wafer flat (the wafer flat was along the $\langle 1-10 \rangle$ direction). The flat had a tolerance of ± 1 deg to the $\langle 1-10 \rangle$ direction and the cutting process had a tolerance of ± 2 deg. Finally, the shear modulus depended on the width to thickness ratio of the cantilever. The combined uncertainty for shear modulus was less than 1% of the nominal shear modulus ($54 \leq G \leq 64.7$).

The cantilever width uncertainty was specified as two times the SWLI lateral resolution ($2 \times 4.4 \mu\text{m}$). Dividing by the cantilever width gives a range from 0.3% to 1.3%. Similarly, cantilever thickness uncertainty was specified as two times the SWLI vertical resolution ($2 \times 2.7 \text{ nm}$) which was negligible for thicknesses of 0.305 and 0.311 mm. However, thickness had a much greater variability when measuring at multiple locations on the same cantilever. Thickness measurements were made by placing a glass slide under the cantilever and measuring from the top of the glass to the top of the cantilever surface. This distance was affected by contaminants between the glass and

cantilever and by variability in wafer thickness. Also, measuring the thickness risked damaging the cantilevers. Therefore, a maximum variability of 9 μm was assumed based on multiple measurements of a few cantilevers at different locations on each cantilever. For a 0.311 mm thick cantilever the uncertainty is 2.9%.

The coefficient matrix used in the force equations was obtained from a least-squares fit to the three-dimensional deformation data, i.e. a series of (x,y,z) points. The uncertainty in the deformation data is related to the uncertainty in the coefficient matrix by the covariant matrix. Rewriting Equation 5-3 more generally,

$$y(x, z) = \underbrace{B_3 f_1(x, z) + B_2 f_2(x, z)}_{\text{bending}} + \underbrace{C_1 f_3(x, z) + C_0 f_4(x, z)}_{\substack{\text{bending} \\ \text{and} \\ \text{torsion}}} + \underbrace{D f_5(x, z) + H f_6(x, z)}_{\text{torsion}} \quad (5-14)$$

a new symmetric matrix, α , can be defined with elements,

$$\alpha_{lk} \stackrel{\text{def}}{=} \sum_{i=1}^n \sum_{j=1}^m \left[\frac{1}{\sigma_{ij}} f_l(x_i, z_j) f_k(x_i, z_j) \right] \quad (5-15)$$

where l and k are the row and column numbers of α respectively and vary from 1 to 6, m is the number of measurements across the width of the cantilever, n is the number of measurements down the length of the cantilever, and $m \times n$ is the total number of measurements. Since measurements are obtained by the SWLI camera, each (x,z) location is a different pixel, where i and j are the pixel indices. The term σ_{ij} is the y-coordinate measurement uncertainty at a given pixel (i,j) and was assumed to be the same for all pixels. This enabled σ to be estimated by,

$$\sigma^2 \cong \frac{1}{N-6} \sum_{i=1}^n \sum_{j=1}^m [y_{ij} - (B_3 x_i^3 + B_2 x_i^2 + C_1 x_i + C_0 + D x_i z_j + H z_j)]^2 \quad (5-16)$$

where $N=n \times m$ and 6 corresponds to the number of free parameters (the coefficients).

The covariant matrix is the inverse of α . The elements of the covariance matrix are the variances and covariances of the fitted coefficients,

$$\alpha^{-1} = \begin{bmatrix} \sigma_{B_3}^2 & \sigma_{B_3}\sigma_{B_2} & \sigma_{B_3}\sigma_{C_1} & \sigma_{B_3}\sigma_{C_0} & \sigma_{B_3}\sigma_D & \sigma_{B_3}\sigma_H \\ \cdot & \sigma_{B_2}^2 & \sigma_{B_2}\sigma_{C_1} & \sigma_{B_2}\sigma_{C_0} & \sigma_{B_2}\sigma_D & \sigma_{B_2}\sigma_H \\ \cdot & \cdot & \sigma_{C_1}^2 & \sigma_{C_1}\sigma_{C_0} & \sigma_{C_1}\sigma_D & \sigma_{C_1}\sigma_H \\ \cdot & \cdot & \cdot & \sigma_{C_0}^2 & \sigma_{C_0}\sigma_D & \sigma_{C_0}\sigma_H \\ \cdot & \cdot & \cdot & \cdot & \sigma_D^2 & \sigma_D\sigma_H \\ \cdot & \cdot & \cdot & \cdot & \cdot & \sigma_H^2 \end{bmatrix} \quad (5-17)$$

A typical result of the covariance matrix using torsion loading of 7.552 g on a 1.46 mm wide by 0.311 mm thick by ~5 mm long cantilever on the positive torque arm is,

$$\alpha^{-1} = \begin{bmatrix} 816.1 & -3.456 & 0.004 & 0.000 & 0.001 & 0.000 \\ \cdot & 0.015 & 0.000 & 0.000 & 0.000 & 0.000 \\ \cdot & \cdot & 0.000 & 0.000 & 0.000 & 0.000 \\ \cdot & \cdot & \cdot & 0.000 & 0.000 & 0.000 \\ \cdot & \cdot & \cdot & \cdot & 0.001 & 0.000 \\ \cdot & \cdot & \cdot & \cdot & \cdot & 0.000 \end{bmatrix} \times 10^{-5} \quad (5-18)$$

with values for $|B_3|$ and $|D|$ of 18.2556 and 0.4874 respectively. Taking $\sqrt{(\alpha^{-1})_{11}}/B_3$ and $\sqrt{(\alpha^{-1})_{55}}/D$ gives the uncertainty in these terms of 0.5% and 0.02% respectively.

The coefficients also had measurement-to-measurement deviation when loaded with the same mass multiple times. Therefore, the standard deviation was computed for every measurement sequence and found to be around 2% of the mean for both B_3 and D . Gravity was assumed to be 9.81 m/s² but alignment to gravity was not checked so a conservative 5 deg deviation was assumed leading to an uncertainty of 0.4% of 9.81 m/s². The torque arms had a minimum uncertainty due to the SWLI lateral resolution (2 x 4.4 μm was used). Additionally, the alignment grooves were used to extrapolate the torque arm distance. Using the extrapolation procedure and comparing to a direct measurement of the torque arm by stitching multiple images together, it was found the torque arm could be off by as much as 100 μm so the uncertainty was set to this limit. Finally, all masses were weighed by a precision balance with a resolution of 0.1 mg so the uncertainty was set to two times this value (2 x 0.1 mg).

CHAPTER 6 CONCLUSIONS

All results under predicted the measured mass (6% to 12%). The thickness was the largest uncertainty contributor at 3% (Table 5-2) providing a 9% uncertainty in the estimated mass compared to the measured mass. This uncertainty alone nearly closes the gap in the under predictions. Thickness measurement is a significant challenge that is not unique to this research. Not only is it difficult to measure, but its uncertainty is amplified by being cubed in the force equation.

For the first torsion study (parameters in Table 5-1), the estimated mass was systematically higher for the positive torque arm than for the negative torque arm (Figures 5-8 and 5-9). This is contrasted with the second torsion study where the opposite trend was observed (Figure 5-11). The reason for the difference is the method for computing the torque arms. In the first torsion study, because many cantilevers were tested, the torque arms were extrapolated based on the alignment grooves. In the second torsion study, the torque arms were directly measured by stitching multiple images together to obtain both the tee and cantilever in a single view. Note that in the first study, the gap between the mean positive torque arm and the mean negative torque arm was 3.8% while in the second study, the gap was 1.3% and in the opposite direction (total difference of 5.1%). The torque arm concept used in this research is analogous to AFM tip height. Determining these values is a significant challenge in cantilever force research.

In the study where the normal force coefficient simultaneously with the torsion force coefficient (Figure 5-10 and Figure 5-11) were computed from a single test, the estimated mass using the normal force could be directly compared to the estimated

mass from the torsional force. The two results both under estimated the measured mass but by different amounts. The normal force under estimated by 8% and the torsion force by 11.9% (difference of 3.9%). Common parameters in the force equations contribute equally and in the same direction to both results and, therefore, the difference must be because of uncommon parameters. For example, shear modulus uncertainty does not contribute to the normal force result but does contribute to the torsion force result.

Summary

Measuring the deflection of an AFM cantilever at a single spatial point requires the use of a scalar stiffness as the force transduction constant. Stiffness, however, is a poorly defined quantity for a cantilever sensing an unknown 3D force vector. If, instead, deflection of the cantilever is measured at multiple points simultaneously, the force vector can be determined unambiguously. Measurements made this way are immune to many of the problems associated with traditional single point measuring schemes. There is no dependency on where the load is applied or what portion of the beam is measured and there is no cubic dependency of measurement location on length. Each force component can be independently determined, whereas, in single point techniques, the total force vector must be decomposed using prior knowledge about the relationships between the force components.

A prototype platform was designed to measure the full-field deflection profile of cantilevers under load. The primary platform component was a scanning white light interferometer (SWLI), which measures surface contours through the low coherence interference of white light. This platform was used to test a new 3D force model. Forces were applied to single crystal silicon cantilevers to cause bending and torsion. From the 3D deformation, the forces were determined unambiguously.

Future Work

This study identifies many follow-on research topics. A natural extension is to validate the model for the third force component, P . Then, the complete force model could be verified using AFM-scale cantilevers. The obvious challenge for micrometer-scale cantilevers is identifying sources of suitably small reference forces and determining the material properties and the thickness of multi-layered cantilevers. Finally, the prototype platform could be improved. For example, the SWLI measurement rate is on the order of seconds. Adapting the SWLI for shorter measurement times or selecting an alternative measurement approach could reduce dynamic disturbances such as vibrations. With a new high frequency measurement transducer, a new dynamic 3D force model could be investigated.

LIST OF REFERENCES

- [1] Langlois E, Shaw G, Kramar J, Pratt J and Hurley D 2007 Spring constant calibration of atomic force microscopy cantilevers with a piezosensor transfer standard *Rev. of Sci. Instrum.* **78** 093705
- [2] Emerson R and Camesano T 2006 On the importance of precise calibration techniques for an atomic force microscope *Ultramicroscopy* **106** 413
- [3] Kim M and Pratt J 2010 SI traceability: Current status and future trends for forces below 10 microNewtons *Measurement* **43** 169
- [4] Matei G, Thoreson E, Pratt J, Newell D and Burnham N 2006 Precision and accuracy of thermal calibration of atomic force microscopy cantilevers *Rev. of Sci. Instrum.* **77** 083703
- [5] Heim L, Kappl M and Butt H 2004 Tilt of atomic force microscope cantilevers: Effect on spring constant and adhesion measurements *Langmuir* **20** 2760
- [6] Wang F 2009 Comment on Influence of atomic force microscope cantilever tilt and induced torque on force measurements *Applied Physics* **106** 096103
- [7] Hutter J 2005 Comment on Tilt of atomic force microscopy cantilevers: effect on spring constant and adhesion measurements *Langmuir* **21** 2630
- [8] Edwards S, Ducker W and Sader J 2008 Influence of atomic force microscope cantilever tilt and induced torque on force measurements *Applied Physics* **103** 064513
- [9] Butt H, Cappella B and Kappl M 2005 Force measurements with the atomic force microscope: Technique, interpretation and applications *Surface Science Reports* **59** 1
- [10] Chung K, Pratt J and Reitsma M 2010 Lateral force calibration: Accurate procedures for colloidal probe friction measurements in atomic force microscopy *Langmuir* **26** 2
- [11] Hutter J and Bechhoefer J 1993 Calibration of atomic-force microscope tips *Review of Scientific Instruments* **64** 7
- [12] Binnig G, Quate C and Gerber C 1986 Atomic force microscope *Physical Review Letters* **56** 9
- [13] Binnig G, Rohrer H, Gerber C and Weibel E 1982 Surface studies by scanning tunneling microscopy *Physical Review Letters* **49** 1
- [14] Göddenhenrich T, Lemke H, Hartmann U and Heiden C 1990 Force microscope with capacitive displacement detection *Vacuum Science and Technology* **8** 1

- [15] Sasaki M, Hane K, Okuma S, Hino M and Bessho Y 1994 Improved differential heterodyne interferometer for atomic force microscopy *Rev. of Sci. Instrum.* **65** 12
- [16] Martin Y, Williams C and Wickramasinghe H 1987 Atomic force microscope-force mapping and profiling on a sub 100-Å scale *Applied Physics* **61** 10
- [17] Schönenberger C and Alvarado S 1989 A differential interferometer for force microscopy *Rev. of Sci. Instrum.* **60** 10
- [18] Sarid D, Iams D and Weissenberger V 1988 Compact scanning-force microscope using a laser diode *Optics Letters* **13** 12
- [19] Sasaki M, Hane K and Okuma S 1994 Shape of the cantilever deflection for the atomic force microscope in force curve measurements *Rev. of Sci. Instrum.* **65** 6
- [20] Meyer G and Amer N 1988 Novel optical approach to atomic force microscopy *Applied Physics Letters* **53** 12
- [21] Tortonese M, Barrett R and Quate C 1993 Atomic resolution with an atomic force microscope using piezoresistive detection *Applied Physics Letters* **62** 8
- [22] Franz C and Puech P 2008 Atomic force microscopy: a versatile tool for studying cell morphology, adhesion and mechanics *Cellular and Molecular Bioengineering* **1** 4
- [23] Kalb J, Spaepen F and Wuttig M 2004 Atomic force microscopy measurements of crystal nucleation and growth rates in thin films of amorphous Te alloys *Applied Physics Letters* **84** 25
- [24] Veerapandian M and Yun K 2009 Study of atomic force microscopy in pharmaceutical and biopharmaceutical interactions – A mini review *Current Pharmaceutical Analysis* **5** 3
- [25] Custance O, Perez R and Morita S 2009 Atomic force microscopy as a tool for atom manipulation *Nature Nanotechnology* **4** 803
- [26] Rosa L and Liang J 2009 Atomic force microscope nanolithography: dip-pen, nanoshaving, nanografting, tapping mode, electrochemical and thermal nanolithography *Physics: Condensed Matter* **21** 483001
- [27] Vettiger P, Cross G, Despont M, Drechsler U, Durig U, Gotsmann B, Harberle W, Lantz M, Rothuizen H, Stutz R and Binnig G 2002 The “millipede” – nanotechnology entering data storage *IEEE Transactions on Nanotechnology* 1/1 p39-55
- [28] Liu H and Bhushan B 2004 Nanotribological characterization of digital micromirror devices using an atomic force microscope *Ultramicroscopy* **100** 391

- [29] Bornschlog T and Rief M 2008 Single-molecule dynamics of mechanical coiled-coil unzipping *Langmuir* **24** 1338
- [30] Brockwell D 2007 Probing the mechanical stability of proteins using the atomic force microscope *Biochemical Society Transactions* **35** 1564
- [31] Ling X, Butt H and Kappl M 2007 Quantitative measurement of friction between single microspheres by friction force microscopy *Langmuir* **23** 8392
- [32] Butt H and Kappl M 2009 Normal capillary forces *Advances in Colloid and Interface Science* **146** 48
- [33] Kopycinska-Müller M, Geiss R and Hurley D 2006 Contact mechanics and tip shape in AFM-based nanomechanical measurements *Ultramicroscopy* **106** 466
- [34] VanLandingham M, McKnight S, Palmese G, Elings J, Huang X, Bogetti T, Eduljee R and Gillespie J 1997 Nanoscale indentation of polymer systems using the atomic force microscope *Adhesion* **64** 31
- [35] Sarid D, Hunt J, Workman R, Yao X and Peterson C 1998 The role of adhesion in tapping-mode atomic force microscopy *Applied Physics A* **66** S283
- [36] Karhu E, Gooyers M and Hutter J 2009 Quantitative friction-force measurement by longitudinal atomic force microscope imaging *Langmuir* **25** 6203
- [37] Ogletree D, Carpick W and Salmeron M 1996 Calibration of frictional forces in atomic force microscopy *Rev. of Sci. Instrum.* **67** 9
- [38] Gibson T, Watson S and Myhra S 1996 Determination of the spring constants of probes for force microscopy/spectroscopy *Nanotechnology* **7** 259
- [39] Poggi M A, McFarland A W, Colton J S and Bottomley L A 2005 A method for calculating the spring constant of atomic force microscopy cantilevers with a nonrectangular cross section *Analytical Chemistry* **77** 1192
- [40] Blank K, Mai T, Gilbert I, Schiffmann S, Rankl J, Zivin R, Tackney C, Nicolaus T, Spinnler K, Oesterhelt F, Benoit M, Clausen-Schaumann H and Gaub HE 2003 A force-based protein biochip *PNAS* **100** 11356
- [41] Cleveland J P, Manne S, Bocek D and Hansma P K 1993 A nondestructive method for determining the spring constant of cantilevers for scanning force microscopy *Rev. of Sci. Instrum.* **64** 403
- [42] Gibson C T, Weeks B L, Lee J R I, Abell C and Rayment T 2001 A nondestructive technique for determining the spring constant of atomic force microscope cantilevers *Rev. of Sci. Instrum.* **72** 2340

- [43] Golovko D S, Haschke T, Wiechert W and Bonaccorso E 2007 Nondestructive and noncontact method for determining the spring constant of rectangular cantilevers *Rev. of Sci. Instrum.* **78** 043705
- [44] Gibson C T, Johnson D J, Anderson C, Abell C and Rayment T 2004 Method to determine the spring constant of atomic force microscope cantilevers *Rev. of Sci. Instrum.* **75** 565
- [45] Sader J E, Pacifico J, Green C P and Mulvaney P 2005 General scaling law for stiffness measurement of small bodies with applications to the atomic force microscope *Applied Physics* **97** 124903
- [46] Notley S M, Biggs S and Craig V S J 2003 Calibration of colloid probe cantilevers using the dynamic viscous response of a confined liquid *Rev. of Sci. Instrum.* **74** 4026
- [47] Butt H and Jaschke M 1995 Calculation of thermal noise in atomic force microscopy *Nanotechnology* **6** 1
- [48] Proksch R, Schäffer T E, Cleveland J P, Callahan R C and Viani M B 2004 Finite optical spot size and position corrections in thermal spring constant calibration *Nanotechnology* **15** 1344
- [49] Torii A, Sasaki M, Hane K and Okuma S 1996 A method for determining the spring constant of cantilevers for atomic force microscopy *Measurement Science and Technology* **7** 179
- [50] Pratt J R, Smith D T, Newell D B, Kramar J A and Whitemton E 2004 Progress toward Système International d'Unités traceable force metrology for nanomechanics *Materials Research* **19** 366
- [51] Aksu S B and Turner J A 2007 Calibration of atomic force microscope cantilevers using piezolevers *Rev. of Sci. Instrum.* **78** 043704
- [52] Holbery J D, Eden V L, Sarikaya M and Fisher R M 2000 Experimental determination of scanning probe microscope cantilever spring constants utilizing a nanoindentation apparatus *Rev. of Sci. Instrum.* **71** 3769
- [53] Cumpson P J, Hedley J and Zhdan P 2003 Accurate force measurement in the atomic force microscope: a microfabricated array of reference springs for easy cantilever calibration *Nanotechnology* **14** 918
- [54] Cumpson P J, Hedley J, Clifford C A, Chen X and Allen S 2004 Microelectromechanical system device for calibration of atomic force microscope cantilever spring constants between 0.01 and 4 N/m *Vacuum Science and Technology A* **22** 1444

- [55] Cumpson P J, Clifford C A and Hedley J 2004 Quantitative analytical atomic force microscopy: a cantilever reference device for easy and accurate AFM spring-constant calibration *Measurement Science and Technology* **15** 1337
- [56] Cumpson P J and Hedley J 2003 Accurate analytical measurements in the atomic force microscope: a microfabricated spring constant standard potentially traceable to the SI *Nanotechnology* **14** 1279
- [57] Gates R S and Pratt J R 2006 Prototype cantilevers for SI-traceable nanonewton force calibration *Measurement Science and Technology* **17** 2852
- [58] Niehues J, Lehmann P, and Bobey K 2007 Dual-wavelength vertical scanning low-coherence interferometric microscope *Applied Optics* **46** 7141
- [59] McSkimin H and Andreatch Jr P 1964 Measurement of third-order moduli of silicon and germanium *Applied Physics* **35** 3312
- [60] Srinath L 1980 Advanced mechanics of solids *Tata McGraw-Hill* p239-241
- [61] Wortman J and Evans R 1965 Young's modulus, shear modulus, and Poisson's ratio in silicon and germanium *Applied Physics* **36** 153
- [62] Bevington P and Robinson D 1992 Data reduction and error analysis for the physical sciences *WCB/McGraw-Hill* p121-123

BIOGRAPHICAL SKETCH

The author was born in Miami, FL, in 1982. In 2001, he started his bachelor's degree at the University of Florida (UF). Before graduation, as part of an undergraduate research fellowship, he worked at the National Institute of Standards and Technology (NIST), the United States standards agency. There, he became interested in small force metrology and afterward worked in this field for his master's degree project. In 2007, he earned his master's degree from UF and then interned at NIST. Later, he started his doctoral degree which extended his master's work to the full three-dimensional force model presented in this study.